MSDE

REVIEW

View Article Online
View Journal | View Issue



Cite this: *Mol. Syst. Des. Eng.*, 2019, 4, 1074

Received 16th October 2019,
Accepted 13th November 2019

DOI: 10.1039/c9me00143c

rsc.li/molecular-engineering

# Protein biomaterials for theranostic applications

Kamia Punia, [a] Jacob B. Kronenberg [a] and Jin Kim Montclare *[abc]

Protein biomaterials have been used for a wide range biomedical applications due to their intrinsic biocompatibility, versatility and higher order structure. Multifunctional theranostic agents fabricated by incorporating the diagnostic modalities and drug payloads in protein nanoformulations have garnered significant attention in recent years. Protein-based theranostic agents manifest high target specificity, enhanced blood circulation and reduce reticuloendothelial system elimination. This review focuses on the fabrication of peptide- and protein-based nanoformulations for imaging guided therapy.



## 1. Introduction

Theranostics is a biomedical field that combines diagnostic and therapeutic modalities into a single platform.[1] It facilitates simultaneous therapy and real-time monitoring of target specificity, pharmacokinetics and efficacy of therapeutic agents.[2] The treatment profile of heterogenous diseases such as cancer varies significantly among patients and at different stages of the ailment.[3] Theranostic agents allow a thorough understanding of molecular phenotype to design the therapeutic regimen suitable for specific individuals.[3] It provides early detection of any adverse effects of treatment to afford enough time for clinicians to alter the therapeutic *modus operandi*.[4] Henceforth, theranostics present immense promise for tuning the drug dosage and frequency to improve efficacy and reduce off-target side effects.[5] These unique properties have garnered significant attention for the development of novel theranostic agents. Various types of theranostic agents have been reported in literature including polymers,[6] liposomes,[7] inorganic nanoparticles,[8] and proteins.[9] Recently, protein-based theranostic agents have especially been an intensively studied area of research.[9]

Proteins are versatile materials that are used by nature to fill myriad roles in living systems.[10] They are predominantly made up of 20 amino acid building blocks, which combine in various ways to give proteins their shape and function. As our knowledge of these natural systems have improved, we gain the ability to design new proteins and peptides that are optimized for certain applications: both through modification of existing natural structures and through top-down design. Manipulation of the same 20 basic building blocks can give rise to things as diverse as structural materials,[11] carriers for small-molecules,[12] and catalysts.[13] Incorporation of non-canonical amino acids further broadens the possibilities that proteins provide.[14] Proteins provide many advantages, especially when working with biological systems. They are easily and precisely synthesized through expression by engineered cells.[10] Unlike synthetic polymers, proteins are monodisperse and comprised of a discrete sequence. The variety of amino acids is able to confer specifically targeted responses to stimuli such as pH, temperature, and the presence of certain molecules. Because they are an omnipresent biomaterial, proteins are also inherently biocompatible, which makes them desirable[15] for use in biomedical applications.[9]

Many of these features make proteins and peptides attractive materials for theranostic applications. Proteins such as trastuzumab[16] and erythropoietin[17] as well as peptides such as insulin[18] may have inherent pharmaceutical value through their interactions with diseased tissue. When designing a medical agent, it is important to consider how it will interact with the body, particularly the immune system. Because they consist of naturally present components, protein materials do not tend to elicit unfavourable reactions, and are easily conjugated to cloaking agents such as poly(ethylene glycol) (PEG) for further stealth.[19] It is also useful in both therapeutic and diagnostic applications to create materials with some kind of stimulus response for greater specificity. Responses can be engineered to be stimuli specific to diseased tissue, such as lowered pH[20] and the presence of certain biomolecules such as fibrin or receptors such as HER-2,[21,22] as well as induced stimuli such as hyperthermia.[23] Peptides also have a propensity for self-assembly that allow them to act as carriers for pharmaceutical agents, especially hydrophobic drugs, which

[a] *Department of Chemical and Biomolecular Engineering, New York University Tandon School of Engineering, Brooklyn, New York, 11201, USA. E-mail: Montclare@nyu.edu*
[b] *Department of Chemistry, New York University, New York, New York, 10012, USA*
[c] *Department of Biomaterials, New York University College of Dentistry, New York, New York, 10010, USA*

may otherwise have poor transport and distribution properties. Because of their many advantages in biological systems, much research is dedicated to developing protein and peptide materials for theranostic applications.

In this review, we focus on protein-based multifunctional theranostic agents including: albumin,[24] ferritin,[25] cell-penetrating peptides,[26] antibodies,[21,27] and recombinant proteins.[28] Protein-based nanocarriers comprising therapeutic agents for the treatment of cancer by various techniques such as chemotherapy,[28] photothermal (PT) therapy,[25] photodynamic therapy (PDT),[29] radiotherapy,[27] and gene therapy[24] are explored (Fig. 1). Along with therapeutic agents, the biomaterials decorated with imaging modalities for simultaneous diagnosis using different techniques including magnetic resonance imaging (MRI),[24] positron emission topography (PET),[30] fluorescence imaging,[31] and photoacoustic (PA) imaging[15] are discussed for their potential applications in cancer theranosis (Table 1).

## 2. Magnetic resonance imaging

MRI is a non-invasive technique that is widely used as a diagnostic modality.[32] The operating principle of MRI involves the use of radio frequency (RF) to excite the surrounding water molecules and subsequently measure the relaxation time of the protons to reach the equilibrium state.[33] Although MRI displays real-time monitoring with high spatial resolution, its poor sensitivity poses a challenge in distinguishing normal tissues from the pathological site.[33] To overcome this limitation, various contrast agents can be employed to enhance the MRI sensitivity.[34] There are the two types of commonly used MRI contrast agents, T1 and T2, based on their working principle (Fig. 2).[33] Upon exposure to external magnetic field, the protons align their spins either parallel or anti-parallel to the magnetic field (Fig. 2A). While alignment, the protons spin at a rate of precession known as Larmor frequency ($\omega_0$). Application of RF pulse to the nuclei causes protons to excite to the antiparallel state by absorbing energy (Fig. 2B). After removal of RF pulse, the nuclei relax to their lower energy state *via* two pathways: longitudinal relaxation (T1 relaxation) and transverse relaxation (T2 relaxation) (Fig. 2C and D). T1 relaxation involves recovering of protons to their initial state with net decrease in magnetization ($M_z$) and in T2 relaxation, dephasing of spins causes a decaying of induced magnetization perpendicular to plane ($M_{xy}$).

T1 contrast agents such as gadolinium-based complexes shorten the longitudinal relaxation time of water protons that leads to brightening of images. T2 contrast agents like superparamagnetic iron oxide nanoparticles (MNPs; <20 nm size) can shorten the transverse relaxation time of water, causing darkening of images. MRI sensitivity can be further increased by conjugating the contrast agents to macromolecules including proteins, monoclonal antibodies, and carbohydrates[47] (*vide infra*). Extensive efforts are underway to explore multifunctional theranostic agents by chemically conjugating or physically entrapping the therapeutic molecules with MRI contrast agents.[48]

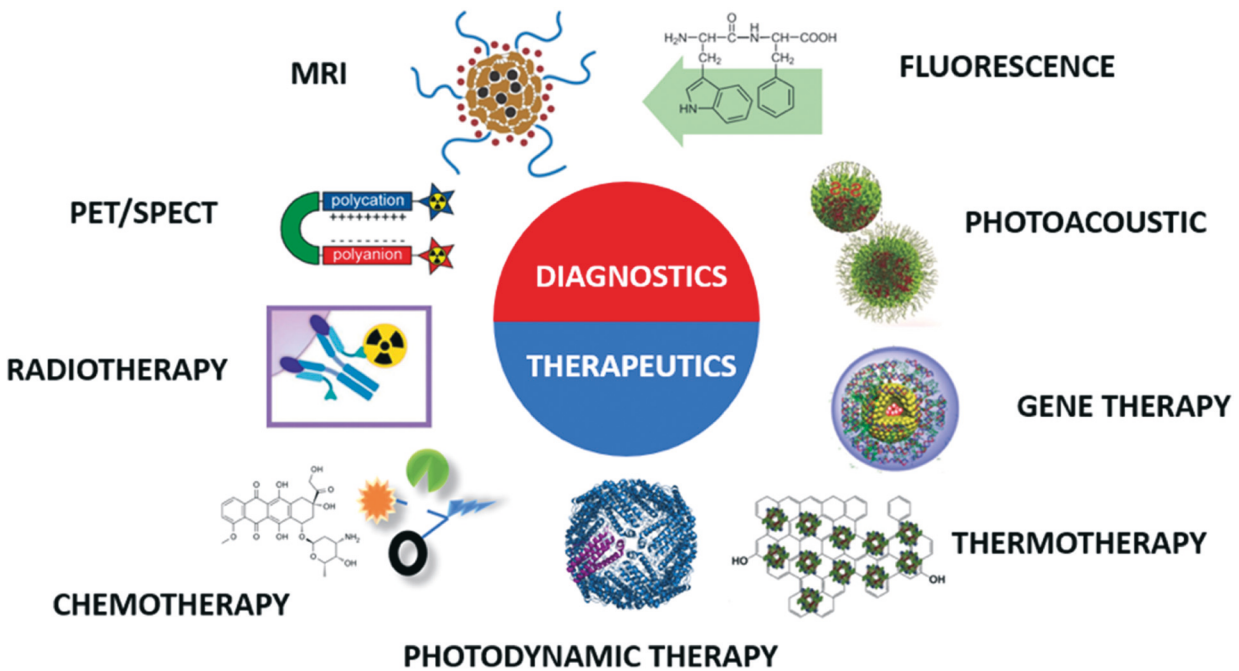


**Fig. 1** Theranostics combine a variety of therapeutic modes such as chemotherapy, radiotherapy, photodynamic therapy, thermotherapy, and gene therapy with diagnostic and imaging modes such as PET/SPECT, MRI, fluorescence imaging, and photoacoustic/ultrasound imaging. Reproduced with permission.[15,24,26,30,31,35,36]

Table 1 Overview of protein-based theranostic agents

| Protein/peptide | Purpose | Diagnostic method | Therapeutic method | Ref. |
|---|---|---|---|---|
| Bovine serum albumin-β-cyclodextrin | Enhance relaxivity and circulation time | Gd-Based MRI | Gene therapy | 24 |
| Bovine serum albumin-$MnO_2$-indocyanine green/paclitaxel | Enhance relaxivity | Mn-Based MRI | Chemotherapy and PT therapy | 37 |
| Fluorinated-thermoresponsive assembled protein (F-TRAP) comprising coiled-coil domain of cartilage oligomeric matrix protein, elastin and RGD domain | $^{19}F$ MRI and tumour targeting | $^{19}F$ MRI and fluorescence from conjugated NIR dye | Chemotherapy *via* encapsulated doxorubicin | 28 |
| Bovine serum albumin-polyethylene glycol | Enhance biocompatibility and circulation time | Superparamagnetic iron oxide magnetic nanoparticles for MRI | Chemotherapy *via* encapsulated doxorubicin | 35 |
| Trp-Phe dipeptide | Fluorescence | Fluorescence from the Trp-Phe peptide | Chemotherapy by conjugated doxorubicin | 31 |
| Octoarginine | Cell-penetrating peptide | Fluorescence from conjugated doxorubicin | Chemotherapy by conjugated doxorubicin | 26 |
| gH625 | Cell-penetrating peptide | Fluorescence from conjugated Cy5.5 and MRI with iron oxide nanoparticles | siRNA for gene therapy | 38, 39 |
| CREKA | Selectivity for fibrin | Fluorescence from Cy7 | Pharmaceuticals carried within the micelles | 40 |
| D-Peptide gels | Structural and drug carrier | Fluorescence from conjugated fluorophore as well as fluorescent side chains | Chemotherapy by conjugated taxol | 41 |
| Biotin receptor/biotin complex | Targeting method | Fluorescence from conjugated fluorescein or PET from $^{18}F$ | Chemotherapy by conjugated taxol and camptothecin | 42, 43 |
| Monoclonal antibodies | Targeting method | SPECT from $^{177}Lu$ | Radiotherapy from $^{177}Lu$ | 27, 21 |
| MMP-cleavable CPPs | Cell-penetrating peptide | SPECT from $^{177}Lu$ and $^{125}I$ | Radiotherapy from $^{177}Lu$ | 30, 44 |
| Bovine serum albumin | Reductant for graphene oxide | Nanosized-reduced graphene oxide for PA imaging | Nanosized-reduced graphene oxide for PT therapy | 15 |
| Ferritin | Encapsulation of NIR dye in ferritin capsule | NIR dye loaded ferritin for PA and fluorescence imaging | NIR dye loaded ferritin for PT therapy | 25 |
| Human serum albumin | Encapsulation of chlorin e6 photosensitizer | Fluorescence and PA from chlorin e6, MRI from $Mn^{2+}$ | Chlorin e6 for PT therapy | 36 |
| Anti-GPC3 antibody | Targeting method | Fluorescence from conjugated IRDye700-DX | Photoimmunotherapy and tandem bound paclitaxel | 45 |

### 2.1 T1-contrast agents

Gadolinium-based paramagnetic contrast agents hold great promise in cancer diagnostics.[49] $Gd^{III}$ ion has high magnetic moment due to the presence of seven unpaired electrons in the f-orbital. However, $Gd^{III}$ exhibits high toxicity in ionic state, impeding its usage as a contrast agent. Chelation of $Gd^{III}$ to multidentate ligands such as 1,4,7,10-tetraazacyclododecane-*N*,*N*′,*N*″,*N*‴-tetraacetic acids (DOTA), diethylenetriaminepentaacetic acid (DTPA), and their derivatives can significantly reduce toxicity.[49] Several $Gd^{III}$ chelates including Gd-DTPA (Magnevist®)[50] and Gd-DTOA (Dotarem®)[51] have been currently used in clinical setting. Although, $Gd^{III}$ chelates exhibit unprecedented functionality as diagnostic carrier, they suffer from low relaxivity and rapid clearance.[52,53] To overcome these limitations, the contrast agents are bound to macromolecules such as proteins,[54] liposomes,[55] and synthetic polymers[56] *via* covalent or non-covalent interactions. Protein–polymer conjugates exhibit properties of both biological and synthetic molecules, that can be tailored independently to display specific functions.[57]

Yuan and co-workers have designed protein–polymer based theranostic agent for gene-delivery and MRI.[24] Cationic supramolecular nanoparticles are generated *via* host–guest interaction of adamantine-modified bovine serum albumin (BSA-Ad) and β-cyclodextrin-cored star ethanolamine-functionalized poly(glycidyl methacrylate) (CD-PGEA), and electrostatic self-assembly of BSA and $Gd^{3+}$ ions. The adamantine moiety is introduced onto BSA *via* amidation to produce BSA-Ad, and CD-PGMA polymers are synthesized by

 

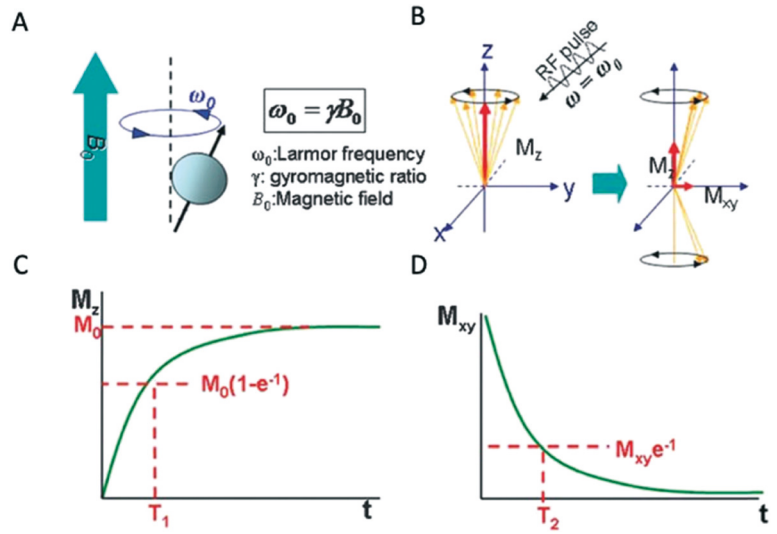


Fig. 2 Principle of magnetic resonance imaging. A) Alignment of protons either parallel or antiparallel to the magnetic field and precess with Larmor frequency ($\omega_0$). B) Upon application of RF pulse, the protons are excited and relaxation takes place upon removal of pulse *via* C) T1 relaxation and D) T2 relaxation. Reproduced with permission from Na *et al.*[46]

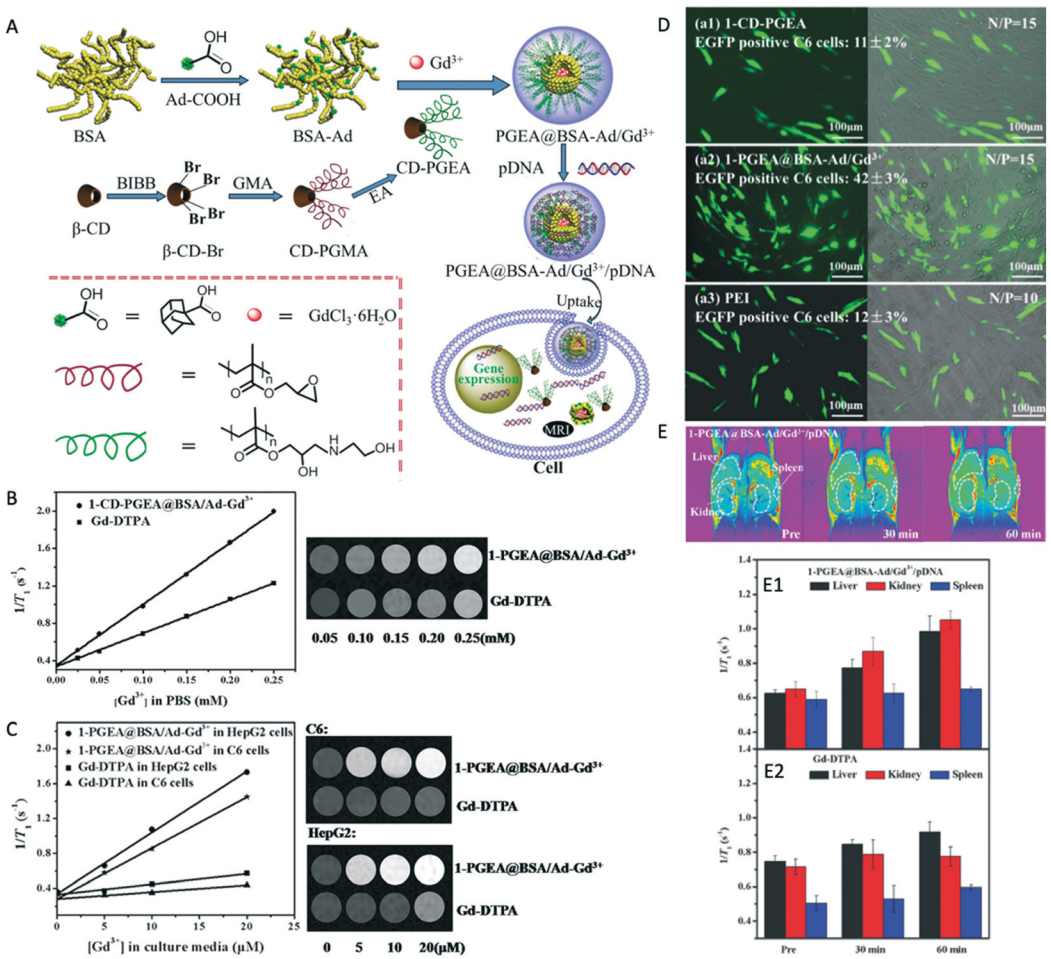


Fig. 3 Protein-based Gd nanoparticles for MRI and gene-delivery. A) Schematic representation for BSA-based supramolecular assemblies, inverse T1 as a function of Gd concentration and T1-weighted MRI of PGEA@BSA-Ad/$Gd^{3+}$ and Gd-DTPA in B) PBS and C) in C6 and HepG2 cells. D) Expression of EGFP by CD-PGEA, PGEA@BSA-Ad/$Gd^{3+}$, and PEI in C6 cells. E) T1-weighted MR images and inverse T1 values of different organs of the mice pre and post injection of E1) 1-PGEA@ BSA-Ad-$Gd^{3+}$/pDNA (1.125 μmol Gd per kg) and E2) Gd-DTPA (1.125 μmol Gd per kg). Reproduced with permission from Yuan *et al.*[24]

atom transfer radical polymerization (ATRP) using the macroinitiator CD-Br and the epoxy groups. CD-PGMA are then subjected to ring opening reaction with ethanolamine to give CD-PGEA (Fig. 3A). Aqueous solutions of CD-PGEA, BSA-Ad, and $Gd^{3+}$ are mixed to create supramolecular self-assembly of PGEA@BSA-Ad/$Gd^{3+}$ into nanoparticles (Fig. 3A). Longitudinal proton relaxation time (T1) of PGEA@BSA-Ad/$Gd^{3+}$ is measured in phosphate buffer saline (PBS) solutions and inverse T1 is plotted as a function of $Gd^{3+}$ concentration (Fig. 3B). T1 weighted MRI of PGEA@BSA-Ad/$Gd^{3+}$ shows significantly brighter images and almost twice the T1 relaxivity as compared to the commercial contrast agent Magnevist (Gd-DTPA). T1 values of C6 and HepG2 cells treated with PGEA@BSA-Ad/$Gd^{3+}$ and Gd-DTPA is considerably higher than PBS solutions due to intracellular enrichment of the agents (Fig. 3B and C).[24] Furthermore, the relaxivity of PGEA@BSA-Ad/$Gd^{3+}$ in C6 and HepG2 cells is significantly stronger than Gd-DTPA treated cells (Fig. 3C), indicating great potential for MRI applications.[24] PGEA@BSA-Ad/$Gd^{3+}$ also exhibits significantly higher gene transfection efficiency of a reporter gene pRL-CMV in C6 and HepG2 cell lines than polyethylenimine (PEI) as control. The gene transfection efficiencies of the complexes are also analyzed using pEGFP-N1 plasmid to visualize the enhanced green fluorescent protein (EGFP) expression in C6 and HepG2 cells. PGEA@BSA-Ad/$Gd^{3+}$ demonstrate considerably higher expression of EGFP in C6/HepG2 cells in comparison to CD-PGEA and PEI (Fig. 3D).[24] *In vivo* studies suggest that the T1-weighted MRI signal intensity and inverse T1 of kidney and liver is enhanced greatly, 60 minutes post intravenous (IV) injection of PGEA@BSA-Ad/$Gd^{3+}$/pDNA whereas no increase in inverse T1 is observed for Gd-DTPA (Fig. 3E). The above results indicate the prolonged *in vivo* circulation time of PGEA@BSA-Ad/$Gd^{3+}$; serving as a potential contrast agent for T1 weighted imaging.

Manganese ($Mn^{2+}$) is also an attractive paramagnetic contrast agent that shortens the T1 relaxation time of water protons to increase the signal intensity of MR images. $Mn^{2+}$ produces the positive contrast signal due to the presence of five unpaired electrons.[58] $Mn^{2+}$ is an essential trace nutritional element that is involved in mitochondrial function, making it a great contrast agent for the organs rich in mitochondria such as liver, pancreas and kidneys.[59] $Mn^{2+}$ form stable chelates with macrocyclic ligands such as dipyridoxal diphosphate (DPDP) and diethylene triamine pentaacetic acid (DTPA).[60] $Mn^{2+}$-DPDP (TeslascanTM) is a clinically approved MRI contrast agent.[61]

Manganese-based multifunctional theranostic nanoplatform has been designed by Pan and co-workers.[37] $MnO_2$ nanoparticles (NPs) are fabricated using BSA as a template as well as a reductant to mimic the disinfection process of $KMnO_4$ (Fig. 4). The aqueous solutions of BSA and $KMnO_4$ are mixed and stirred for 2 hours to generate $MnO_2$ NPs templated on BSA as the product of the redox reaction. The facile synthesis strategy produces highly monodisperse BSA-$MnO_2$ (BM) NPs of sub-10 nm size with excellent T1 relaxivity (7.9 $mM^{-1}$ $s^{-1}$), which is higher than Gd-DTPA (4.6 $mM^{-1}$ $s^{-1}$).

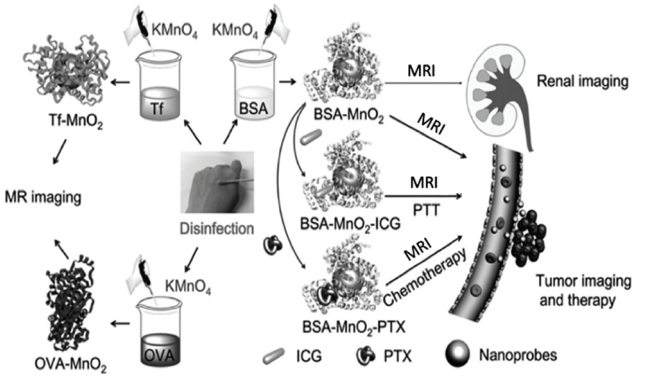


Fig. 4 Manganese-based T1 contrast agent. Schematic representation of the synthesis of $MnO_2$ NPs-based theranostic agent by mimicking disinfection process and their applications in MR imaging (MRI) of tumour and renal imaging as well as image-guided chemotherapy and PT therapy of tumors. Reproduced with permission from Pan *et al.*[37]

Photothermal (PT) therapy is a minimally invasive technique for cancer treatment that employs heat from absorption of light in near-infrared (NIR) wavelength range (700–2000 nm) to cause tumour ablation.[62] Therapeutic agents, indocyanine green (ICG) for PT therapy and paclitaxel (PTX) as a chemotherapeutic agent are loaded onto the hydrophobic domain of BSA by mixing them with BM NPs to generate two theranostic agents: BSA-$MnO_2$-ICG (BMI) and BSA-$MnO_2$-PTX (BMP) (Fig. 4). BMI NPs demonstrate highest relaxivity (70 $mM^{-1}$ $s^{-1}$) of all available T1 contrast agents. *In vivo* administration of BMI in tumour-bearing mice exhibit substantial tumour ablation with laser irradiation as compared to the control mice (administered with PBS plus laser irradiation; BM NPs plus laser irradiation; BMI NPs without laser irradiation). Chemotherapeutic ability of BMP NPs is assessed *in vivo* by injecting it in mice bearing 4T1 tumors. BMP NPs significantly inhibit the growth of tumour, whereas mice treated with PBS or free PTX exhibit an increase in tumour growth with time. To evaluate universality of this strategy, the MR nanoprobes have been successfully fabricated with other functional proteins including ovalbumin and transferrin. The BM NPs fabricated by facile disinfection-mimicking strategy serves as a promising multifunctional nanoplatform for MRI diagnosis and therapy.

### 2.2 T2-contrast agents

Fluorine-19 ($^{19}F$) MRI is another imaging technique that has gained recent attention in biomedical applications.[63–65] including tumour imaging,[66,67] monitoring tumour cell growth,[67,68] cell tracking,[69] and monitoring enzymatic activity.[70,71] $^{19}F$ is an attractive candidate for MRI due to its 100% natural abundance and high NMR sensitivity (83% of $^{1}H$ sensitivity).[63] Fluorine is present in negligible amount in the body except in teeth and bones, which does not produce

 

signal with conventional MRI.[64,72] This lack of background signal allows enhancement of signal with increase in concentration of introduced fluorine. Commonly used fluorinated agents for MRI include perfluorocarbons (PFCs) such as perfluoropolyether (PFPE), perfluoro-15-crown-5-ether (PFCE) and perfluorooctyl bromide (PFOB), which serve as T2 darkening agents.[73,74] For its applications in NMR and MRI, $^{19}$F probes can be introduced into the peptides and proteins *via* solid-state synthesis,[75] site-specific[76] or residue-specific[77] incorporation.

The Montclare group has biosynthesized fluorinated thermoresponsive assembled protein (F-TRAP) that forms micelles capable of visualization by $^{19}$F MRI and MRS.[28] The thermoresponsive assembled protein (TRAP) is designed to have an RGD sequence for tumour targeting, coiled-coil domain of cartilage oligomeric matrix protein (C) that self-assembles into α-helical bundles, and elastin-like polypeptide (E) region comprised of a $[(VPGVG)_2VPGFG(VPGVG)_2]_2$ repeat that demonstrates an inverse transition temperature (Fig. 5A).[28] $^{19}$F is introduced in the protein *via* residue-specific incorporation of trifluoroleucine (TFL) to produce F-TRAP, which assembles into micelles of ~30 nm at 20 °C as assessed by dynamic light scattering (DLS) and transmission electron microscopy (TEM). A dramatic increase in size (952.06 ± 300.17 nm) is observed upon raising the temperature to 50 °C, demonstrating the thermoresponsive behaviour of protein. Both TRAP and F-TRAP have shown the ability to encapsulate the chemotherapeutic agent doxorubicin (Dox), and behave in a thermoresponsive fashion to release the drug due to thermally induced coacervation of proteins. Assessment of *in vitro* therapeutic efficacy of the Dox-loaded protein micelles suggests enhanced drug release to MCF-7 breast adenocarcinoma cells under hyperthermic conditions, leading to significant reduction in cell viability at 42 °C as compared to physiological temperature conditions.

Zero echo time (ZTE) $^{19}$F MRI pulse was used to prevent signal loss due to short T2 relaxation time while assessing the diagnostic ability of F-TRAP. ZTE $^{19}$F MRI scans conducted on both F-TRAP (21.9 mM $^{19}$F) sample and water as a control generated positive signals for $^{1}$H nuclei. $^{19}$F signal was achieved from F-TRAP within 1 hour of acquisition time. Fluorescence microscopy and $^{19}$F MRS were performed for *in vivo* detection of intratumorally injected NIR dye-

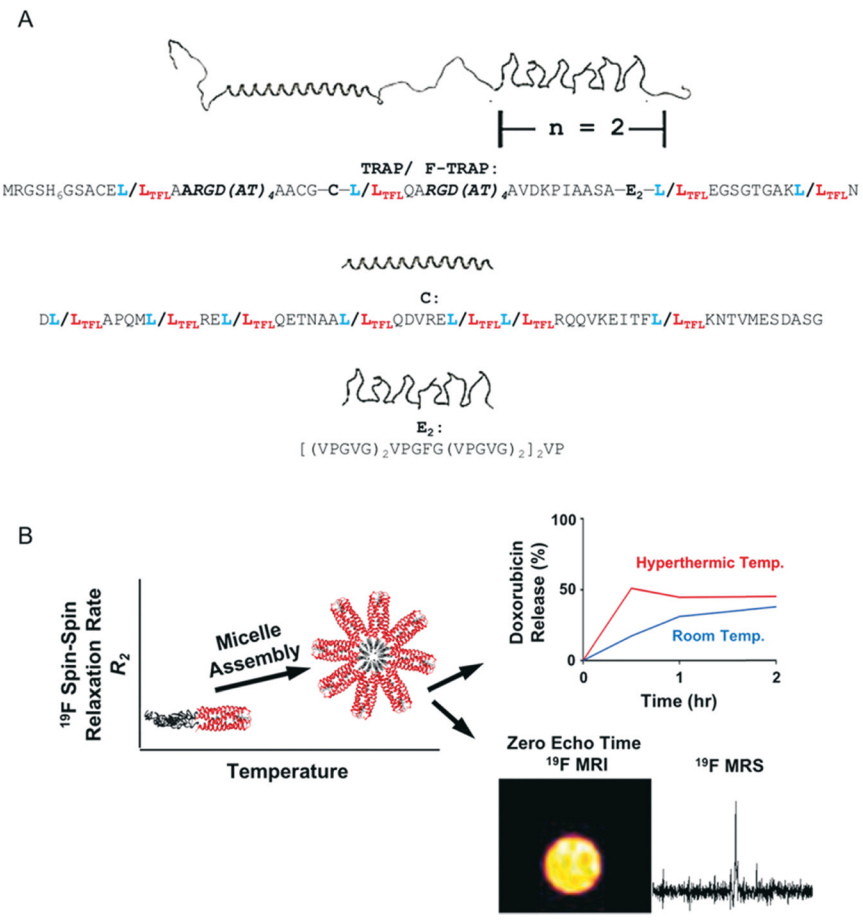


**Fig. 5** Fluorinated thermoresponsive protein block copolymers for $^{19}$F MRI. (A) TRAP monomer and sequence showing the coiled-coil (C) domain and elastin-like polypeptide (E) domain. F-TRAP results by replacing leucine (L, blue) with trifluoroleucine (TFL, red). (B) Schematic representation of F-TRAP assembly, thermoresponsive drug release, and detection by $^{19}$F MRS and by zero-echo time (ZTE) $^{19}$F MRI when sufficient fluorine is present. Reprinted with permission from Hill *et al.* Copyright 2019 American Chemical Society.[28]

conjugated F-TRAP. Significant $^{19}F$ MRS signal could be obtained within 7 minutes after injection in a mouse model (Fig. 5B). This work signified the potential of self-assembling protein biomaterials as multifunctional therapeutic and diagnostic agent.

Superparamagnetic iron oxide magnetic nanoparticles (SPION) have been extensively studied as a diagnostic agent and a therapeutic carrier.[78] SPION range from 10–100 nm in size that allows passive tumour targeting by enhanced permeability and retention (EPR) effect and to escape the reticuloendothelial system (RES) of the body.[79,80] SPION have been extensively used for visualizing tumors in liver, spleen and lymph nodes to allow diagnosis in early stages.[81–83] SPION mainly act as a negative MRI contrast agent by shortening T2/T2* relaxation time leading to darkening of the imaging site.[78] However, due to its poor biocompatibility, low drug loading capacity and propensity to aggregate, its application in biomedical field is hindered.[84] Efforts have been made to overcome these limitations by coating the SPION with biocompatible materials, including dextran,[85] chitosan,[86] polyethyleneimine[87] and serum albumin.[88] In one study, Semkina *et al.* have designed pH responsive core–shell corona $Fe_3O_4$ nanoparticles (MNPs) loaded with Dox for theranostic applications.[35] MNPs are synthesized by thermal decomposition of iron acetylacetonate(III) in benzyl alcohol. BSA shell is adsorbed onto the $Fe_3O_4$ core followed by cross-linking by glutaraldehyde to improve stability. Polyethylene glycol (PEG) corona is subsequently coated onto MNPs-BSA nanoparticles by carbodiimide chemistry (Fig. 6A). The BSA shell binds to the anticancer drug Dox and the PEG corona improves the biocompatibility and stability and reduces the RES elimination. The MNP-BSA@Dox-PEG nanoparticles show high T2 relaxivity values (270 ± 6 $mM^{-1}$ $s^{-1}$), demonstrating its potential as an MRI contrast agent. 3-(4,5-Dimethylthiazol-2-yl)-2,5-diphenyl tetrazolium bromide (MTT) cell viability assay has been performed to assess the therapeutic efficiency of the BSA@Dox-PEG nanoparticles. The complex exhibits similar cytotoxicity against C6 and HEK293 cells as the free Dox (Fig. 6B). The results indicate BSA@Dox-PEG complex is a promising bifunctional therapeutic and diagnostic agent.

Cell-penetrating peptides (CPPs) are peptides first identified in HIV that readily undergo receptor-independent uptake into cells.[89] A common motif in CPPs is the arginine oligomer. It is known that cationic peptides are able to cross the cell membrane and it is believed that the positively charged guanidine group of arginine confers this ability to penetrate the cell.[90] CPPs also allow intake through non-destructive mechanisms, meaning that their cargo is less likely to be damaged while entering the cell.[89] Because they do not rely on expression of a particular receptor and are able to carry a variety of cargos, they are versatile candidates for delivery of drugs and contrast agents.[89] However, their versatility also leads to a high rate of off-target effects. It is

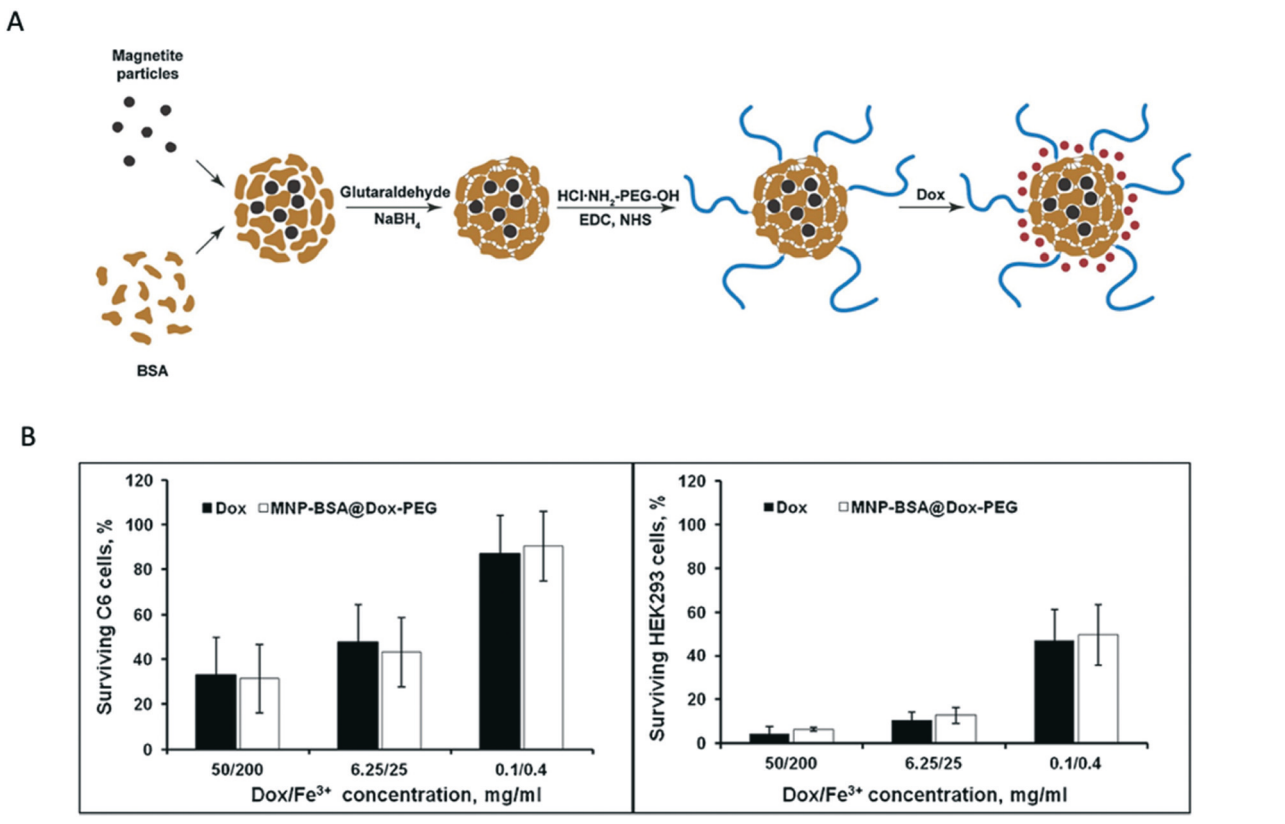


**Fig. 6** Core–shell–corona doxorubicin-loaded MNPs. A) Schematic of synthesis of BSA@Dox-PEG nanoparticles. B) MTT cell viability assay for MNP-BSA@Dox-PEG nanoparticles and Dox in C6 and HEK293 cells. Reproduced with permission Semkina *et al.*[35]

 

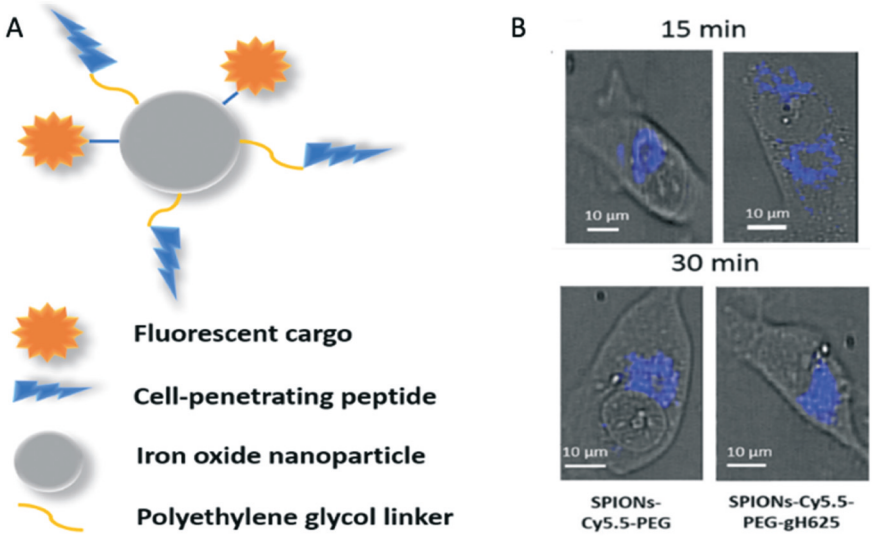


**Fig. 7** A) A schematic showing the iron oxide SPION core conjugated to PEG linkers bearing both CPPs and fluorescent cargo. B) Sample *in vivo* fluorescence images for SPIONs with and without attached CPPs. Those with CPPs showed approximately twice the fluorescence intensity. Reproduced with permission from Perillo *et al.*[38]

therefore important to have some sort of activator or trigger to ensure that the CPPs only actively release the drug in affected areas.

Perillo *et al.* report the creation of theranostic SPION coated with PEG and the CPP gH625.[38] These nanoparticles have iron oxide cores that are conjugated to two linkers. One linker is used to attach the fluorophore Cy5.5 to enable fluorescence imaging. The other linker is used to attach PEG, which minimizes immune response to the nanoparticles (Fig. 7).[19] Click chemistry is used to attach the cationic CPP gH625 to the surface. Conjugating CPPs to the nanoparticles improves their uptake into human breast cancer cells by greater than three times. In addition to fluorescence imaging, MRI is possible because iron oxide nanoparticles are innately useful as magnetic contrast agents.

PEGylated SPION have previously been shown to function as effective MRI contrast agents.[91] More recent research has shown that addition of polyarginine allows these nanoparticles to act as siRNA delivery vectors with greater efficacy than commercially available liposomal vectors.[39]

MRI is a powerful diagnostic technique with the ability to penetrate deep into tissues while offering high resolution images. T1 and T2 contrast agents are being widely used in clinical MRI to improve the contrast between normal and diseased tissues. Conjugation/encapsulation of contrast agents to macromolecules such as proteins can greatly enhance the relaxivity, systemic circulation, and tumour targeting at lower dosage. Protein-based MRI contrast agents have shown immense potential in theranostics as exemplified from aforementioned studies focusing on $Gd^{III}$ and $Mn^{II}$-

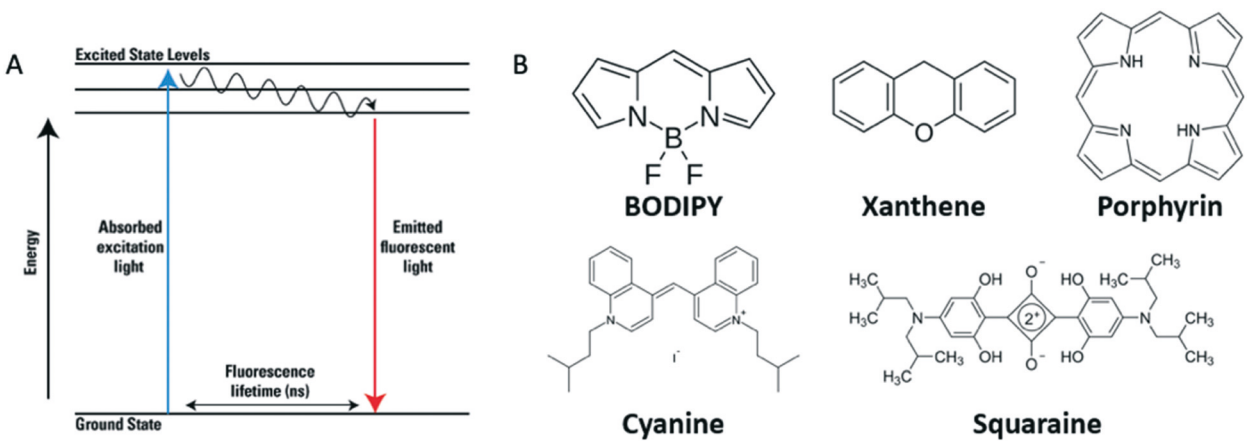


**Fig. 8** A) A diagram showing the process of excitation and emission giving rise to fluorescence. B) The base structures of several common fluorophores. Precise absorption and excitation wavelengths as well as further chemical functionality may be tuned through the addition of side groups.[93]

based T1 contrast agents and $^{19}F$ and SPION-based T2 agents.[24,28,35]

## 3. Fluorescence imaging

Fluorescence is a process involving emission of light from an excited molecule. When a photon strikes a receptor molecule, or fluorophore, its energy can be absorbed and excite an electron. The excited electron then drops down to the ground state and releases a photon with an energy corresponding to the difference between ground and excited states (Fig. 8A).[92] Because a molecule's electrons have discrete excited states, each fluorophore has a unique fluorescence signature. This specificity makes them useful as imaging agents because high contrast and specificity can be achieved by monitoring signal from wavelengths corresponding to the fluorophore's signature. Fluorophores tend to have multiple conjugated aromatic rings (Fig. 8B).[92] Some biomaterials may have intrinsic fluorescence, for example tryptophan-containing proteins, but most rely on extrinsic fluorescence, in which fluorophore moieties are attached to or complexed with the biomaterial. Because fluorophores can be easily attached to a variety of biomolecules, they are a good candidate for medical imaging probes. Past work has allowed for imaging by attaching fluorophores to cell-penetrating peptides,[89] liposomes and lipoproteins,[94] and antibodies.[95] Current work applying fluorescent imaging in a clinical setting often focuses on NIR (700–1000 nm) fluorophores because of its ability to penetrate deeper into tissue allowing for greater imaging range.[96] NIR fluorophores in clinical use most often include cyanine derivatives such as cyanine 7 and indocyanine green.[96] Other clinically applied fluorophores include porphyrin derivatives[97] (Fig. 8B).

Intrinsically fluorescent proteins such as green fluorescent proteins (GFP) have found wide use because of their highly visible fluorescence and biocompatibility.[98] They are, however, susceptible to denaturing due to changes in temperature and pH, which significantly reduces fluorescence. Fan *et al.* have designed and synthesized intrinsically fluorescent, self-assembling dipeptide nanoparticles (DNPs), which are temperature- and pH-stable while showing bright fluorescence (Fig. 9).[31] Past research has shown that GFP's fluorescence is improved by π–π stacking between tryptophan and phenylalanine residues in its barrel[99] as well as through complexation with Zn(II) (Fig. 9A and B).[100] Trp-Phe dipeptides have been designed to self-assemble into nanoparticles around Zn(II) ions (Fig. 9C). The DNPs' inherent fluorescence is improved upon self-assembly. They do not exhibit photobleaching unlike organic dyes such as rhodamine 6G and they have a minimal effect on cellular viability, unlike fluorescent quantum dots. Cell-surface associated mucin 1 (MUC1) aptamers have been conjugated to the surfaces of the particles, allowing them to target overexpressed MUC1 receptors on the surfaces of tumour cells. The DNPs are able to bind the chemotherapeutic drug, Dox, through π–π stacking with the dipeptide residues resulting in quenching of fluorescence. As the Dox is released, the quenching is undone, and both Dox and the DNPs regain fluorescence, allowing for live imaging of drug delivery and release (Fig. 9D). The dipeptides provide

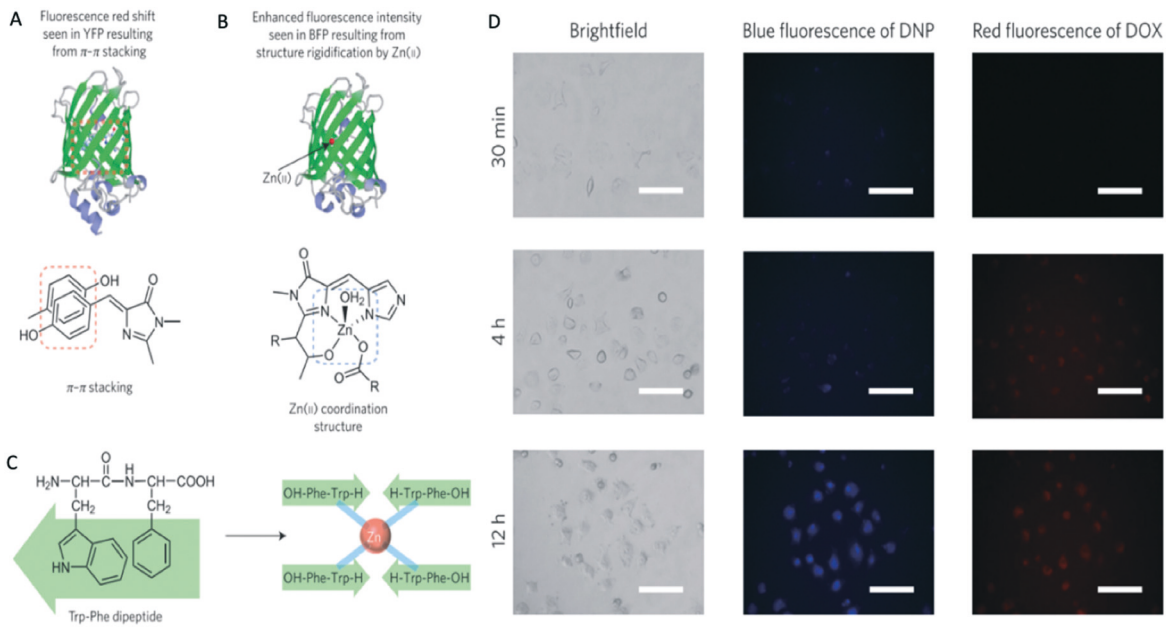


**Fig. 9** Trp-Phe dipeptides self-assemble into fluorescent nanoparticles with the ability to bind and release doxorubicin. A) The structure of YFP showing the importance of π–π stacking for fluorescence. B) The structure of BFP showing that Zn(II) improves fluorescence. C) The structure of DPN monomers and nanoparticles. D) Fluorescence microscopy images showing the release of Dox from DPN over time in MUC1+ tumour cells. Reproduced with permission from Fan *et al.*[31]

 

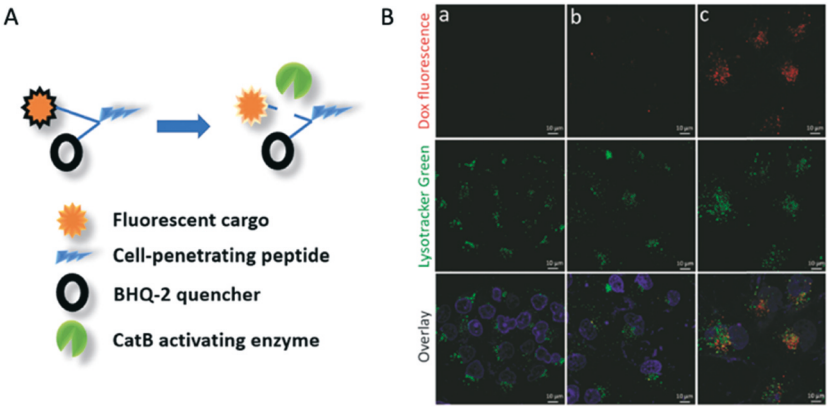


**Fig. 10** CPP-functionalized carriers capable of improving the cellular uptake of a wide variety of theranostic cargos. A) Cartoon schematic showing the design of delivery of quenched fluorescent Dox by CPP with a locally activatable linker.[26] B) Fluorescence images showing Dox fluorescence and a stain showing cell death as well as an overlay demonstrating the correspondence with no drug (a), free Dox (b), and Dox with CPP (c). Reproduced with permission from Lock *et al.*[26]

numerous advantages over other conventional fluorophores and the DNPs are a promising agent for monitored drug delivery.

Lock *et al.* have developed a peptide-based system for the delivery and simultaneous monitoring of the chemotherapeutic drug Dox using fluorescence imaging.[26] Dox is an anthracycline drug that is known to show fluorescence. This is useful when tracking the presence of Dox in the patient's system, but it does not give information about drug delivery. To develop a method to monitor intracellular delivery, Dox is first linked with Black Hole Quencher-2 (BHQ-2), a molecule that absorbs in the same range that Dox fluoresces, thus quenching the signal (Fig. 10A). The BHQ-2 is attached with a GFLG peptide. This sequence is known to be cleaved by the lysosomal protease cathepsin B, so upon entering the tumour cell, the BHQ-2 will detach. The Dox-BHQ-2 complex is covalently bound to the well-established CPP octoarginine (R8) to form the Dox-BHQ-2-R8 complex.[89] This allows for the imaging of Dox that has been successfully delivered and released to the cells. The Dox-BHQ-2-R8 complex successfully quenches the fluorescence of Dox and is cleaved by cathepsin B. Fluorescence imaging with this probe is used to track Dox delivery in drug-resistant ovarian cancer cells (Fig. 10B), demonstrating its effectiveness for monitoring during therapy.

Self-assembling protein materials have an incredibly broad range of uses.[10] The Tirrell group has reported a peptide material which self-assembles into micelles with a diameter of approximately 8 nm.[40] These micelles consist of PEG conjugated to the fibrin-binding peptide CREKA, which confers selectivity, and the fluorophore cyanine-7 (Cy7). Particles, including micelles, are able to target tumours due to the EPR effect, by which nanoparticles tend to accumulate in irregular tumour vasculature to a far greater degree than in healthy tissue.

This effect, combined with the selectivity for fibrin, which is often present around lesions, allows these particles to successfully target glioblastoma in mouse models with minimal cytotoxicity. Fig. 11 shows *in vivo* fluorescence imaging comparing the peptide micelles with bare Cy7. The micelles demonstrate a much higher concentration and remain visible after 24 hours but are cleared within a week.

It also shows a comparison between tumour cells and a brain injury model, demonstrating that the imaging is selective for tumour lesions, not simply damaged tissue.

Fluorophores can also be used as therapeutic agents in their own right, as in the photoimmunotherapy (PIT) techniques reported recently by the Kobayashi group.[45,101] PIT is a technique in which the patient is treated with NIR fluorophores conjugated to antibodies that bind with some receptor on the membranes of tumour cells, allowing for

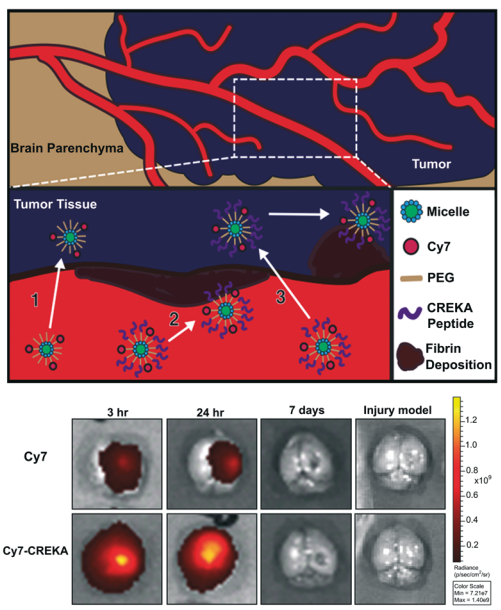


**Fig. 11** A schematic shows the entry mechanisms of delivery micelles with and without fibrin-targeting CREKA oligopeptides.[40] Fluorescence microscopy images display the differences between targeted micelles carrying targeted Cy7 and plain Cy7 are compared at various timepoints as well as in a non-tumour brain injury model. Reproduced with permission from Chung *et al.*[40]

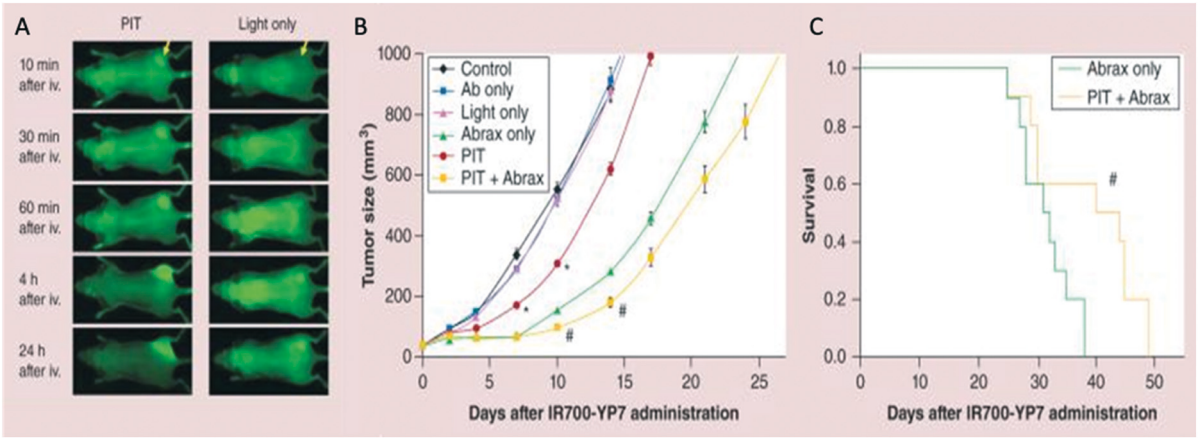


**Fig. 12** A) Fluorescence images of tumour-bearing mice with and without targeting antibodies showing localization of fluorophores to tumour regions post intravenous (iv) injection. B) A plot showing the effect of PIT, Abrax, and tandem therapies on hepatic cell carcinoma tumour growth. C) Comparison of survival of tandem-treated mice with mice treated only with Abrax. Reproduced with permission from Hanaoka *et al.*[45]

targeting and localization. When exposed to NIR light, the fluorophores act as sensitizing agents and disrupt the tumour cell's membranes, resulting in necrotic cell death. PIT treatment not only kills tumour cells, but also increases permeability of the tumour to drugs. A therapy has been developed taking advantage of this effect to treat a murine model of hepatocellular carcinoma.[45] In this treatment, the NIR fluorophore IRDye700-DX is conjugated to an antibody that binds the overexpressed Glypican-3 receptor and administered to tumour-bearing mice *via* IV injection. The tumours are exposed to NIR light and nanoparticular albumin-bound paclitaxel (Abrax) is administered. Because of the increased permeability of the tumour after NIR, a higher degree of nanoparticle accumulation is observed in the tumour (Fig. 12A). The tandem therapy also outperforms both simple PIT and simple administration of Abrax in terms of suppressing tumour growth and improving mouse survival (Fig. 12B and C).[45]

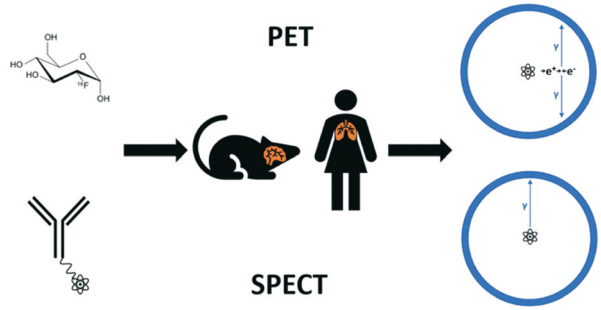


**Fig. 13** A schematic showing the processes of PET and SPECT. First a radionuclide is attached to some sort of tracer, often a biologically active molecule or a targeting antibody. Then, the tracer is injected into the patient or model. The tracer localizes to the area of interest, allowing for imaging. In PET, a positron is emitted, which annihilates with a neighbouring electron giving off a pair of photons with opposite momentum. In SPECT, a single photon is emitted during decay. These are imaged using detectors at various angles around the site and give a three-dimensional tomographic image.

Fluorescence has proven useful in theranostic applications, both for monitoring the release of inherently fluorescent drugs such as Dox as well as imaging fluorescent delivery agents. Fluorescent theranostic agents can consist of dyes conjugated to known drug delivery mechanisms such as capsules[25] and CPPs[26] or inherently fluorescent vehicles. Fluorescence remains an important imaging tool because of its low cost and versatility, allowing for the development of a variety of new agents.

## 4. Positron emission tomography and single-photon emission computed tomography

PET is a medical imaging technique by which cross-sectional, or tomographic, images are created by measuring γ-radiation resulting from the annihilation of positrons emitted by radionuclide tracers (Fig. 13).[102] When they decay, certain radionuclides emit positrons, which annihilate upon encountering an electron and release two γ-rays of equal energy in opposite directions. A γ-ray detector registers a large number of photon pairs allowing for the creation of a distribution map showing the frequency of positron emissions, which corresponds to the concentration of the radiotracer in the tissues being imaged. Although it uses ionizing radiation, PET is a safe technique because the radionuclides are present in concentrations as low as nanomolar, so the patient is not exposed to significant risk from radiation.[102] Because there is a very low amount of background radiation of the type detected by PET scans, the technique allows for high-quality images. However, since PET images the decay events rather than the positron emission itself, there is a limitation placed on resolution by the energy of the positrons emitted; higher-energy positrons travel further from the radiotracer on average before causing γ-ray emission.[102] Higher image quality can be achieved when

 

using smaller radionuclides, which result in lower-energy emission.

Single-photon emission computed tomography (SPECT) is a related imaging technique that also uses radionuclide tracers (Fig. 13).[102] Like PET, SPECT relies on the administration of a radioactive tracer to the patient with some factor allowing it to differentiate among the tissues being imaged. However, rather than monitoring pairs of γ-ray photons, SPECT monitors single photons being emitted by radioactive nuclei. In order to achieve a three-dimensional image, SPECT scanners take measurements from many angles and calculate the internal distribution of radiation sources (Fig. 13). Because of the ease of obtaining γ-ray emitting nuclides), SPECT is cheaper than PET, but it does not have as high image contrast.[103] SPECT can also be used with a variety of therapeutic radionuclides.

Radionuclides that are commonly used for medical imaging include $^{11}$C, $^{18}$F, $^{99m}$Tc, and $^{89}$Zr.[104] $^{18}$F in particular has seen wide use, as it substitutes easily for hydrogens or hydroxide groups in biological molecules. Biological activity can be measured using radiotagged analogs of relevant molecules.[105] For example, since tumours have abnormally high rates of glucose uptake and glycolysis, it is helpful to monitor glucose metabolism. This is done using the radiotracer [$^{18}$F]-(FDG), which is taken in by cells in a similar manner to glucose. PET with $^{18}$F-FDG is widely used clinically as a diagnostic technique for various types of cancer.[105] One drawback of $^{18}$F-FDG is that it is not tumour-specific, but rather reflects glucose metabolism rates. It can therefore be difficult to distinguish tumours from other tissues with high rates of glucose usage, such as tissues undergoing non-tumour related inflammation or healthy brain tissue.[106] More specific imaging agents show great promise in overcoming these problems.

Biotin is a vitamin and important cofactor involved in a number of important metabolic processes. It has been shown that the most important transporter for biotin is overexpressed in many aggressive cancer cell lines (BR+ lines), so biotin may be used to target diagnostics and therapeutics biotin for such cancers.[107] Vineberg *et al.* have demonstrated the efficacy of linking biologically-derived chemotherapeutic molecules to biotin to combine the former's anti-tumour properties with the latter's specificity (Fig. 14).[42] A tripartite linker has been used to link a taxoid and camptothecin, two anti-tumour drugs with distinct and complementary modes of action, with biotin. The drugs are attached with a linker designed to be cleaved by reaction with the tripeptide glutathione, whose concentration is elevated up to three orders of magnitude in tumour cells relative to the bloodstream, allowing for doubly selective delivery (Fig. 14A). The biotin-conjugated drug reveals a selectivity of greater than two orders of magnitude for cell lines that overexpress the biotin receptor relative to those which did not (Fig. 14B). Further work aims to exploit the previously designed tripartite linkers to create a theranostic conjugate containing biotin as a targeting agent, a taxoid as an active anti-tumour agent, and either an $^{18}$F-containing moiety as a PET agent or fluorescein to allow for fluorescence imaging.[43]

The modularity of this approach allows for a variety of theranostics to be created by mixing and matching targeting agents such as biotin and folate, chemotherapeutic agents such as camptothecin and taxoids, and tracers for various imaging modalities. In spite of the size of these conjugates, they are taken up into cells at comparable rates to plain biotin, meaning that they accumulated in BR+ cells but not in healthy cells. This allows for selective imaging of BR+ tumours with only minimal accumulation outside of the tumour.

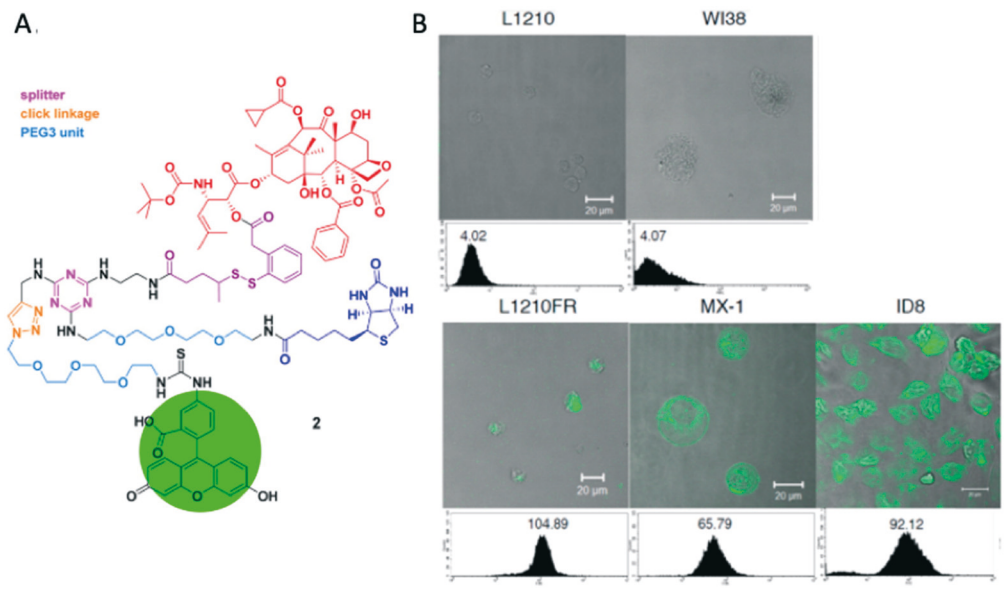


**Fig. 14** A) A schematic of the tripartite targeted molecule containing biotin, a chemotherapeutic taxol, and a fluorophore. B) Flow cytometry images showing high uptake of the molecule in three BR+ cell lines and two BR- cell lines.

Monoclonal antibodies (mAbs) are biomolecules derived from naturally occurring immunoglobulins that exhibit highly specific binding.[108] Certain mAbs are currently widely used in chemotherapy because of their ability to slow tumour growth. For example, trastuzumab is effective against HER2+ tumours including many breast cancers as well as some ovarian and oesophageal cancers.[16] Because of their selectivity and versatility, mAbs show great potential both for application in targeted delivery of therapeutics and as imaging contrast agents. However, their stability in the blood and slow clearing from the body pose a problem when they are conjugated to the radionuclides used for radiotherapy or PET/SPECT imaging. It is important to keep the ratio of off-target radiation to on-target radiation as low as possible. Since the blood is sensitive to radiation, the presence of radionuclides in the blood for prolonged periods of time can be harmful, so strategies must be found to minimize radiation exposure.

Cheal *et al.* have demonstrated a strategy to use bifunctional mAbs for SPECT-based theranostics while minimizing the patient's exposure to radiation.[27] Bifunctional mAbs are antibodies that have an affinity to two different antigens or to an antigen and a hapten. This allows mAbs to be used to link molecules with very high specificity. In pretargeted radioimmunotherapy, a bifunctional mAb with an affinity to some antigen presented on the tumour surface is injected into the patient and allowed to bind with the tumour. Then, a radiolabeled antigen or hapten to which the mAb also has an affinity is injected. The labeled species binds to the mAb, localizing the radionuclides in the tissue of interest and allowing the unbound labeled species to be cleared from the blood much more quickly than would be possible with a radiolabeled mAb. First, in order to target colorectal cancer, an antibody against glycoprotein A33 (GPA33), which is overexpressed in some tumours, is used along with the hapten *S*-2-(4-aminobenzyl)-1,4,7,10-tetraazacyclododecane tetraacetic acid (DOTA) complexed with the $^{177}$Lu radionuclide (Fig. 15A).[27] $^{177}$Lu is chosen because it is active as both a radiotherapeutic agent and as a SPECT tracer, allowing for simultaneous treatment and imaging of the tumours. The bifunctional mAb is administered, followed by a hapten promoting clearance from the mice's vascular systems. This ensures that the only antibody present is that which has bound to tumour cells. Then, the radiotagged $^{177}$Lu-DOTA is administered, binding to the antibodies (Fig. 15B). SPECT scans are performed at

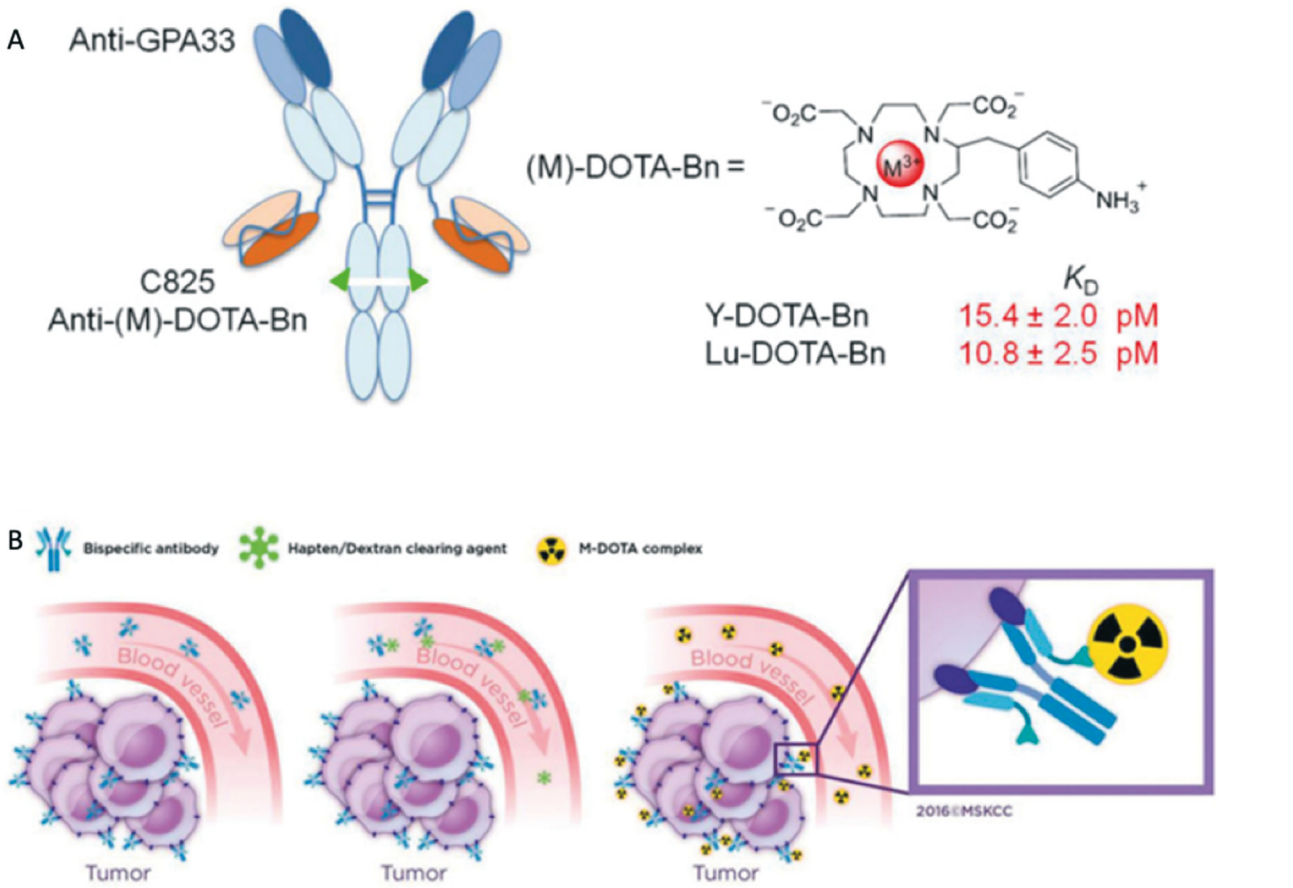


**Fig. 15** Bifunctional antibodies allow targeting through pre-treatment, which significantly improves radionuclide targeting. A) Schematic of a bifunctional monoclonal antibody along with its radio-tagged DOTA-Bn hapten.[27] B) Model of the pre-targeted radiotherapy and SPECT system, reproduced with permission from Cheal *et al.*[27]

 

six time points during the study, showing that there is sufficient local retention of $^{177}$Lu-DOTA for it to be useful as an imaging agent even six days after administration. Mice that received the full treatment exhibit complete cure and 100% survival rates whereas mice that received no treatment or only $^{177}$Lu-DOTA treatment dies after an average of 19 days and 16 days, respectively. Excess $^{177}$Lu-DOTA is excreted renally and no lasting adverse health effects are observed. More recent studies have proven this strategy versatile: a similar study has been conducted using a bifunctional antibody carrying the IgG sequence from mAb trastuzumab, which binds to the HER-2 receptor overexpressed in 30% of all breast cancers.[21] Trastuzumab is known to slow tumour growth and is widely used as a chemotherapeutic agent. This system allows for simultaneous diagnostic ability through SPECT as well as two mechanisms of therapy, namely the trastuzumab-based antibody action and $^{177}$Lu radiotherapy. The two studies show similar results: after three rounds of treatment, mice with tumours showed a 100% survival rate. Additionally, for mice with small tumours, a single round of treatment is sufficient. The usage of engineered bifunctional antibodies is a promising direction for combining nuclear medicine and cancer treatment.

As discussed earlier, cell-penetrating peptides are a versatile tool allowing for the delivery of diverse cargos into the cell. Further research is currently being performed to expand the use of CPPs to include the targeted delivery of radionuclides.[30] For example, Van Duijnhoven *et al.* have synthesized MMP-activatable CPPs carrying $^{177}$Lu-DOTA, which contains a radionuclide that is effective both as radiotherapy and as a SPECT agent, on their arginine-rich arm, as well as $^{195}$I on their glutamate-rich arm allowing for visualization of the CPP activation (Fig. 16). Upon entry into tumour cells expressing MMP-2/9, the linker between the arginine-rich and glutamate-rich arms is cleaved, allowing the delivery of $^{177}$Lu to the cell. Studies on murine models of fibrosarcoma and breast carcinoma have been performed. Although the CPPs are able to deliver radiotherapy to the tumours, distribution of the radionuclide is not exclusive to the tumour. In particular, the spleen and liver show quantities of $^{177}$Lu, suggesting that some cleavage of the peptide occurs in the blood. Functionalized activatable CPPs are promising candidates for delivery of a wide variety of therapeutic and diagnostic agents, but work remains in improving their targeting specificity.

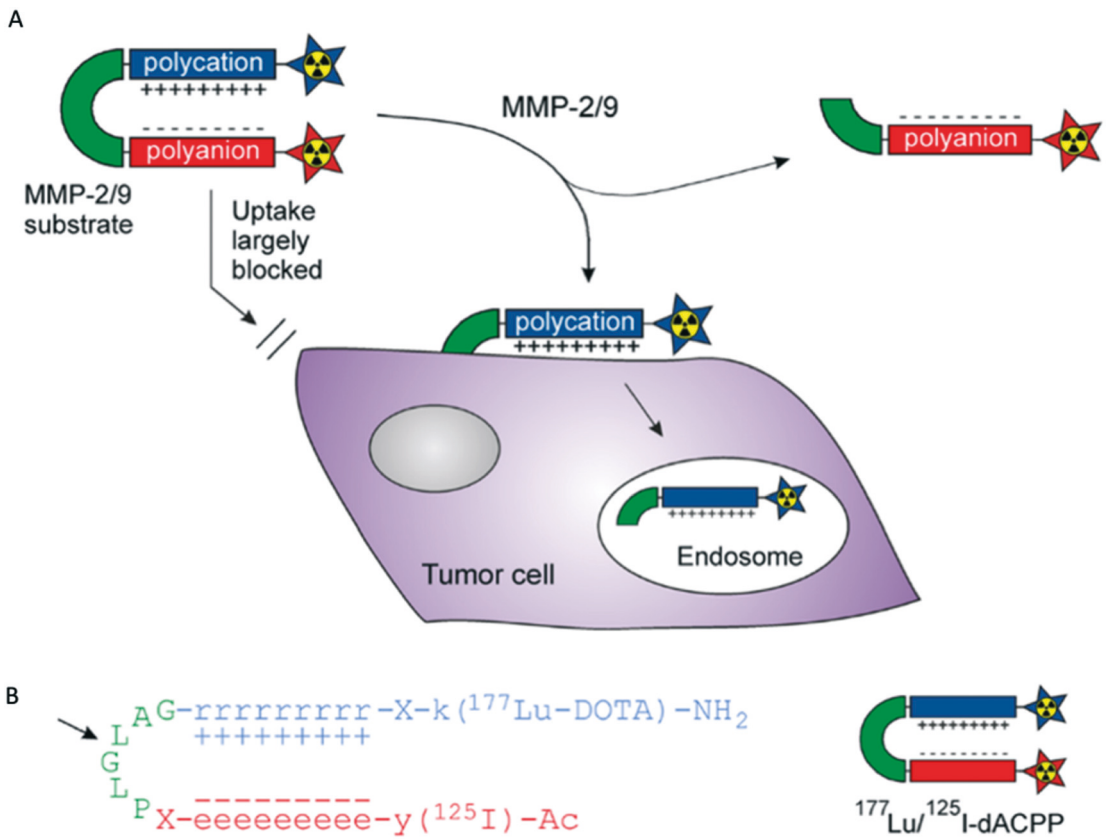


**Fig. 16** CPPs bounded to anionic inhibitory domains can undergo selective cleavage for specific delivery of theranostic agents into cells. A) A schematic of the activation of a radiolabeled CPP by matrix metalloprotein enzymes allowing it to enter the cell. B) The peptide sequence used, showing the poly-arginine CPP, the poly-glutamate neutralizing region, and the MMP-cleavable linker. Reproduced with permission from Van Duijnhoven *et al.*[30]

Radiological imaging techniques such as PET and SPECT are exciting due to their versatility and specificity. Because of their potentially dangerous nature, work must be done to ensure that patient exposure to radiation is as low as reasonably achievable, so much work focuses on improving the targeting of radionuclides. Other work focuses on incorporating radionuclides into known drug delivery mechanisms for imaging, or the promising potential to pair radiological imaging with anti-tumour radiotherapy.

## 5. Photoacoustic imaging

Photoacoustic (PA) imaging is an emerging biomedical diagnostic technique that performs real-time monitoring with high depth of penetration and spatial resolution in the absence of ionizing radiations.[109] In PA imaging, absorption of short-pulsed laser by endogenous chromophores in the body such as melanin or haemoglobin, causes heat generation that leads to thermoelastic expansion of tissues. The tissues then produce acoustic signals that are absorbed by ultrasound transducer. PA imaging using endogenous contrast has been studied for a range of applications including cancer and diabetics. However, generally cancer cells have low PA contrast, requiring exogenous contrast agents for enhancing the PA signal. The exogenous contrast agents absorb in the NIR region (700–1100 nm), where the absorption of tissues is least in order to avoid the background PA signal from endogenous tissues. There are a number of PA contrast agents that have been studied extensively for biomedical applications including NIR dyes such as Alexa Fluor 750,[110] methylene blue, and indocyanine green,[111] graphene and its derivatives,[112] as well as gold and silver nanoparticles.[113] Exogenous contrast agents can be associated with peptides, proteins, and antibodies to target the lesion site, thereby enhancing the photoacoustic signal.[114,115]

Graphene is a material possessing several fascinating properties including high surface area, strong infrared absorption, high mechanical strength and thermal conductivity.[116] Intensive research efforts have been made to explore the biomedical applications of graphene and its derivatives as a drug-delivery vehicle, PA and PT agent for diagnosis and therapy.[117] Sheng and co-workers have fabricated protein based nanosized-reduced graphene oxide (nano-rGO) for PA imaging and PT therapy.[15] BSA being a natural reductant in alkaline condition, is used for reduction and stabilization of graphene oxide (Fig. 17A).

Functionalization of graphene oxide with BSA leads to enhanced UV-vis NIR absorption and subsequently demonstrates an increase in temperature to 55 °C upon 5 min laser irradiation (808 nm). The temperature achieved is higher than required for photoablation, indicating its

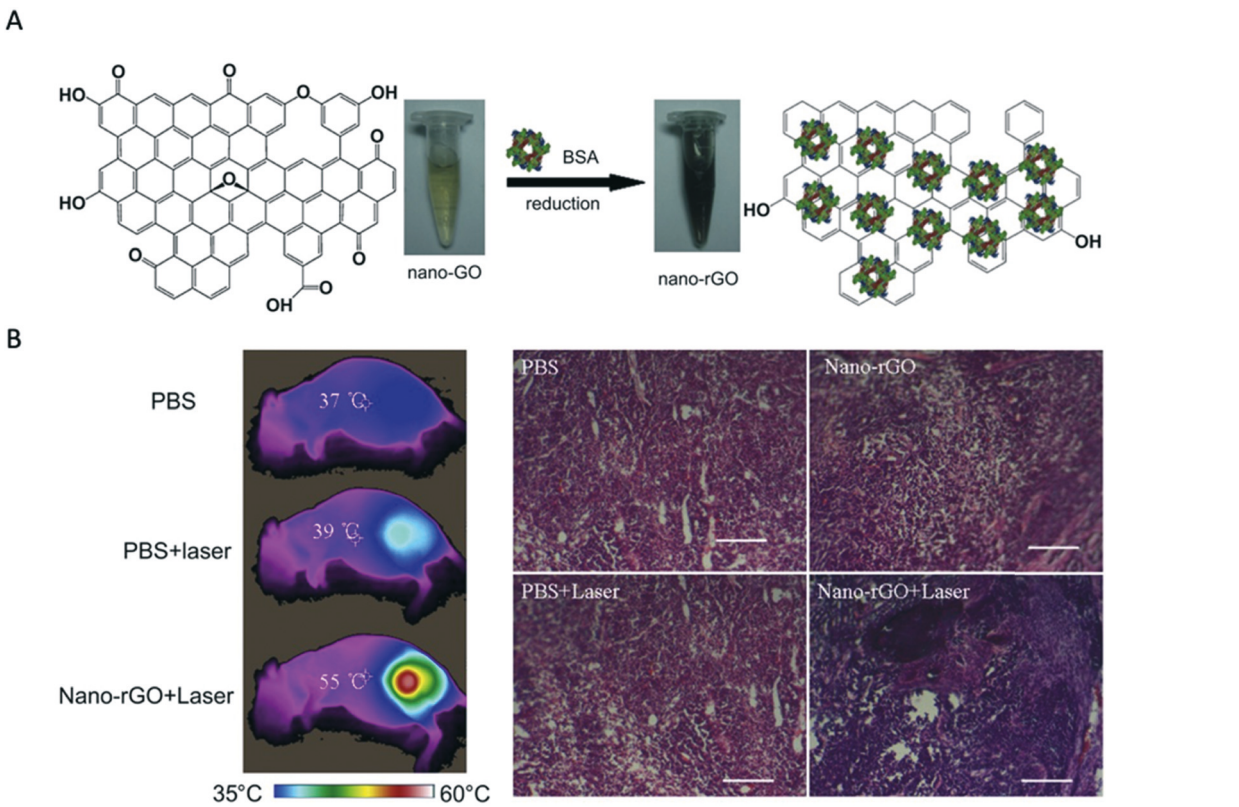


Fig. 17 Nano-reduced graphene oxide for PA imaging and PT therapy. A) Schematic representation of the preparation of nano-rGO by reducing nano-GO using BSA. B) Infrared thermographic maps of mice in different conditions and histological staining of the excised tumors. Reproduced with permission from Sheng *et al.*[15]

 

potential in PT therapy. *In vivo* administration of nano-rGO shows significant signal in tumour region only 30 minutes after IV injection and lasts for up to 4 hours, indicating long retention time in tumour. *In vivo* assessment of photothermal efficacy of nano-rGO using NIR laser displays an increase in temperature by 16 °C after 2 hours of injection, inducing irreversible tissue damage (Fig. 17B). The results suggest that BSA functionalized nano-rGO are promising PA and PT agents.

Ferritin (FRT) is an iron storing protein composed of 24 subunits that self-assemble into a cage-like structure.[118] The quaternary structure of FRT assembles and dissembles with variation in pH, maintaining a stable cage architecture at physiological conditions. FRT cavities have been used to encapsulate various molecules such as cisplatin and desferrioxamine by the virtue of assembling and disassembling its structure.[119] Huang *et al.* have reported NIR dye loaded FRT (DFRT) nanocages for multimodal PA/fluorescence imaging and PT therapy.[25] The IR 820 dye molecules have been loaded into the FRT cavity by opening and closing of FRT nanocages with step wise change in pH from 2 to 7.4. DFRT exhibits remarkable absorbance in the NIR region due to strong interaction between the dye and FRT. DFRT shows a temperature rise of 28.38 °C upon exposure to 1 W $cm^{-2}$ 808 nm laser for 5 minutes, significantly higher photothermal conversion efficiency than FRT and IR 820 dye. Investigation into *in vitro* PT therapeutic efficiency and cytotoxicity of DFRT demonstrates direct relationship between laser dose and PT effect of cells with almost no viable cells present when exposed to 1 W $cm^{-2}$ NIR laser for 5 minutes.

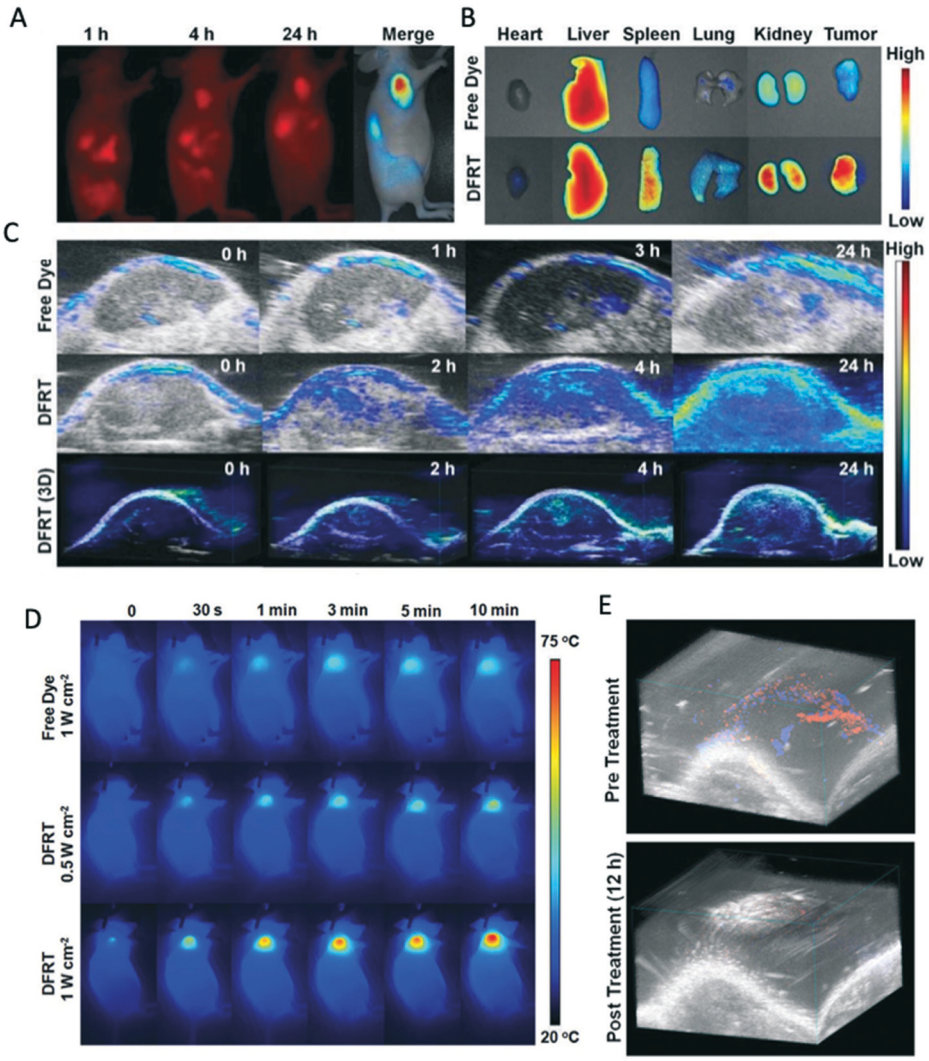


**Fig. 18** NIR dye loaded ferritin nanocages for PA/fluorescence and PT therapy. A) *In vivo* NIR fluorescence images in mice at various intervals after DFRT injection. B) *Ex vivo* NIR fluorescence images of DFRT in mouse tissues. C) *In vivo* cross-sectional ultrasound and PA images of tumour tissues in mice taken at different times after DFRT injection or IR820 dye alone. D) Thermal images of tumour in mice post administration of IR 820 dye or DFRT and exposure to 808 nm laser irradiation. E) 3D color Doppler images of tumour pre and post 12 h PT therapy. Reproduced with permission from Huang *et al.*[25]

Theranostic capability of DFRT is also tested *in vivo* by IV injection. The average fluorescence intensity and PA signals from the tumour suggest that the rate of accumulation of DFRT is significantly higher than the dye alone (Fig. 18A–C). DFRT exhibits significant rise in tumour temperature within 10 minutes of laser irradiation (0.5 or 1 W $cm^{-2}$) with no increase in temperature on other body parts (Fig. 18D). Decimation of blood vessels of tumour has been observed after PT treatment as shown in 3D color doppler images (Fig. 18E). Noteworthy delay in tumour growth has been observed 2 weeks after PT treatment (0.5 W $cm^{-2}$ laser for 10 minutes) with both DFRT and the dye alone. Moreover, DFRT with laser irradiation exhibits complete tumour ablation with no sign of reoccurrence. FRT based multimodal fluorescence/PA imaging guided PT therapy manifests unprecedented opportunities for theranostic applications.

PDT is another therapeutic technique that has shown great promise in clinical setting.[120] Its principle involves irradiation of light onto photosensitizing agent to convert the oxygen present in the tissues to highly reactive oxygen species (ROS) that leads to tumour cell death.[121] Despite the non-invasive nature of PDT, it faces certain challenges including poor tumour selectivity and inadequate oxygen supply in solid tumours leading to low ROS generation that subsequently causes low therapeutic efficiency.[122] These limitations can be overcome by increasing the supply of oxygen in tumour microenvironment.[123] PDT's efficiency can be improved by combining it with PT therapy.[124]

In one of the strategies, oxygen supply in tumour was enhanced by designing thermally modulated human serum albumin-chlorin e6 photosensitizer nanoassemblies (HSA-Ce6 NAs).[36] To generate the HSA-Ce6 assemblies, first the disulfide bonds of HSA are cleaved by glutathione (GSH) and then, Ce6 is loaded onto HSA *via* hydrophobic interactions during self-assembly of HSA by intermolecular disulfide crosslinking. No change in Ce6 absorbance has been observed upon encapsulation. However, fluorescence is triggered after reduction with GSH owing to change in morphology of HSA-Ce6 NAs from spherical to small pieces, illustrating excellent response to reduction. Variation in body temperature of mice from 37 °C to 43 °C leads to an increase in rate of photosensitization, improvement in the supply of oxygen in tumour, and consequently enhancement of PDT efficiency. HSA-Ce6 NAs exhibited significantly enhanced PA signal as compared to free Ce6 after 24 h injection (Fig. 19B), implying a highly efficient tumour accumulation.

HSA-Ce6 NAs can be further chelated with $Mn^{2+}$ to produce triple multimodal theranostic agent (HSA-Ce6–$Mn^{2+}$) with intrinsic fluorescence, PA and MRI capabilities. Enhanced T1 signals of tumour have been observed from HSA-Ce6 NAs than Ce6 alone (Fig. 19B). Aforementioned results demonstrate a promising theranostic platform for imaging-guided PDT. PA imaging has proven to be a valuable tool in pre-clinical research owing to its non-ionizing nature, deep tissue penetration, and marginal signal interference from endogenous tissues. A wide range of exogenous contrast agents have been explored to meet key parameters such as optimum absorption spectrum, low toxicity, and ability to bind targeting moieties.[125] The examples of protein-based PA imaging guided therapy discussed above have demonstrated tremendous potential for the development of advanced theranostic agents.

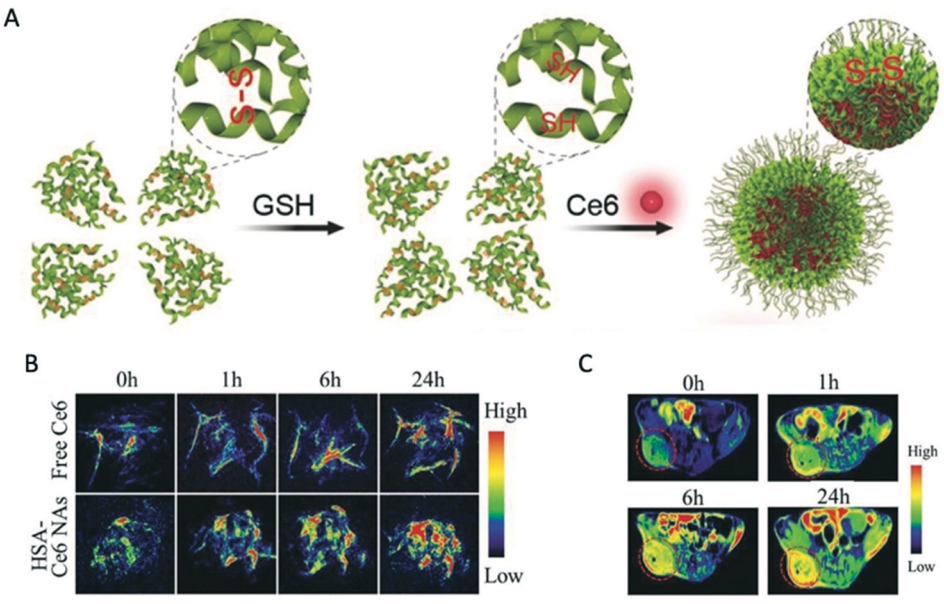


**Fig. 19** HSA-Ce6 photosensitizer nanoparticles for PDT. A) Schematic representation of self-assembly of HSA incorporating Ce6 in the presence of GSH. B) *In vivo* photoacoustic images of the mice bearing 4T1 tumour after injection of free Ce6 and HSA-Ce6 NAs. C) *In vivo* MRI images of the mice bearing 4T1 tumour after injection of HSA-Ce6–$Mn^{2+}$ nanoparticles at different time points. Reproduced with permission.[36]

 

## 6. Conclusions

This review highlights recent advancements in the field of protein-based platforms for imaging-guided therapy. Protein-based biomaterials present exciting opportunities in cancer theranostics due to their intrinsic biocompatibility and multiple physical/chemical binding sites for encapsulation/conjugation of therapeutic and diagnostic agents. Furthermore, protein-based supramolecular assemblies significantly enhance tissue specificity and *in vivo* circulation of theranostic agents. Numerous protein-based systems have been designed for various therapeutic modalities such as chemotherapy, PT therapy, radiotherapy, gene therapy and diagnostic techniques including fluorescence imaging, PET, PA, and MRI. High resolution images at cellular level can be achieved *via* fluorescence imaging, whereas MRI, PET, and PA contrast agents are beneficial for *in vivo* applications due to lower background signal.[1] The concentration of drugs required for a therapy is much higher than the imaging agent. Synergistic integration of diagnostic and therapeutic modalities into a single platform can be obtained by optimizing the concentration of payloads after taking into consideration the limit of maximum tolerance and minimum effectiveness of dose.[126] Additionally, higher diagnostic precision and therapeutic efficacy can be achieved by designing theranostic agents with multi-imaging/therapeutic modalities.[28,127] Imaging-guided therapy could further enable selection and planning of treatment at an early stage of disease, displaying its potential for personalized medicine.[5]

## Conflicts of interest

There are no conflicts to declare.

## Acknowledgements

This work was supported by NSF-DMREF under Award Number DMR 1728858 and NSF-MRSEC Program under Award Number DMR 142007.

## Notes and references

1 S. S. Kelkar and T. M. Reineke, *Bioconjugate Chem.*, 2011, **22**, 1879–1903.
2 B. T. Luk, R. H. Fang and L. Zhang, *Theranostics*, 2012, **2**, 1117–1126.
3 B. Sumer and J. Gao, *Nanomedicine*, 2008, **3**, 137–140.
4 G. Bartlett, J. Antoun and N. K. Zgheib, *Expert Rev. Mol. Diagn.*, 2012, **12**, 841–855.
5 T. Lammers, F. Kiessling, W. E. Hennink and G. Storm, *Mol. Pharmaceutics*, 2010, **7**, 1899–1912.
6 N. Kamaly, Z. Xiao, P. M. Valencia, A. F. Radovic-Moreno and O. C. Farokhzad, *Chem. Soc. Rev.*, 2012, **41**, 2971–3010.
7 Y. Xiuli and D. Zhifei, *Curr. Med. Chem.*, 2018, **25**, 1397–1408.
8 H. Sharma, P. K. Mishra, S. Talegaonkar and B. Vaidya, *Drug Discovery Today*, 2015, **20**, 1143–1151.
9 Q. Chen and Z. Liu, *Adv. Mater.*, 2016, **28**, 10557–10566.
10 Y. Wang, P. Katyal and J. K. Montclare, *Adv. Healthcare Mater.*, 2019, **8**, 1801374.
11 A. J. Olsen, P. Katyal, J. S. Haghpanah, M. B. Kubilius, R. Li, N. L. Schnabel, S. C. O'Neill, Y. Wang, M. Dai, N. Singh, R. S. Tu and J. K. Montclare, *Biomacromolecules*, 2018, **19**, 1552–1561.
12 L. Yin, C. Yuvienco and J. K. Montclare, *Biomaterials*, 2017, **134**, 91–116.
13 A. J. Olsen, L. A. Halvorsen, C. Y. Yang, R. Barak Ventura, L. Yin, P. D. Renfrew, R. Bonneau and J. K. Montclare, *Mol. BioSyst.*, 2017, **13**, 2092–2106.
14 A. Rezhdo, M. Islam, M. Huang and J. A. Van Deventer, *Curr. Opin. Biotechnol.*, 2019, **60**, 168–178.
15 Z. Sheng, L. Song, J. Zheng, D. Hu, M. He, M. Zheng, G. Gao, P. Gong, P. Zhang, Y. Ma and L. Cai, *Biomaterials*, 2013, **34**, 5236–5243.
16 G. Von Minckwitz, M. Procter, E. De Azambuja, D. Zardavas, M. Benyunes, G. Viale, T. Suter, A. Arahmani, N. Rouchet, E. Clark, A. Knott, I. Lang, C. Levy, D. A. Yardley, J. Bines, R. D. Gelber, M. Piccart and J. Baselga, *N. Engl. J. Med.*, 2017, **377**, 122–131.
17 V. Cernaro, G. Coppolino, L. Visconti, L. Rivoli, A. Lacquaniti, D. Santoro, A. Buemi, S. Loddo and M. Buemi, *Med. Res. Rev.*, 2019, **39**, 427–460.
18 R. Ismail and I. Csóka, *Eur. J. Pharm. Biopharm.*, 2017, **115**, 257–267.
19 I. Ekladious, Y. L. Colson and M. W. Grinstaff, *Nat. Rev. Drug Discovery*, 2019, **18**, 273–294.
20 M. Karimi, M. Eslami, P. Sahandi-Zangabad, F. Mirab, N. Farajisafiloo, Z. Shafaei, D. Ghosh, M. Bozorgomid, F. Dashkhaneh and M. R. Hamblin, *Wiley Interdiscip. Rev.: Nanomed. Nanobiotechnol.*, 2016, **8**, 696–716.
21 S. M. Cheal, H. Xu, H. F. Guo, M. Patel, B. Punzalan, E. K. Fung, S. G. Lee, M. Bell, M. Singh, A. A. Jungbluth, P. B. Zanzonico, A. Piersigilli, S. M. Larson and N. K. V. Cheung, *Theranostics*, 2018, **8**, 5106–5125.
22 J. G. Croissant, D. Zhang, S. Alsaiari, J. Lu, L. Deng, F. Tamanoi, A. M. Almalik, J. I. Zink and N. M. Khashab, *J. Controlled Release*, 2016, **229**, 183–191.
23 D. Y. Furgeson, M. R. Dreher and A. Chilkoti, *J. Controlled Release*, 2006, **110**, 362–369.
24 H. Yuan, C. Xu, Y. Zhao, B. Yu, G. Cheng and F.-J. Xu, *Adv. Funct. Mater.*, 2016, **26**, 2855–2865.
25 P. Huang, P. Rong, A. Jin, X. Yan, M. G. Zhang, J. Lin, H. Hu, Z. Wang, X. Yue, W. Li, G. Niu, W. Zeng, W. Wang, K. Zhou and X. Chen, *Adv. Mater.*, 2014, **26**, 6401–6408.
26 L. L. Lock, Z. Tang, D. Keith, C. Reyes and H. Cui, *ACS Macro Lett.*, 2015, **4**, 552–555.
27 S. M. Cheal, E. K. Fung, M. Patel, H. Xu, H. F. Guo, P. B. Zanzonico, S. Monette, K. D. Wittrup, N. K. V. Cheung and S. M. Larson, *J. Nucl. Med.*, 2017, **58**, 1735–1742.
28 L. K. Hill, J. A. Frezzo, P. Katyal, D. M. Hoang, Z. Ben Youss Gironda, C. Xu, X. Xie, E. Delgado-Fukushima, Y. Z. Wadghiri and J. K. Montclare, *ACS Nano*, 2019, **13**, 2969–2985.

29 C. Jiang, H. Cheng, A. Yuan, X. Tang, J. Wu and Y. Hu, *Acta Biomater.*, 2015, **14**, 61–69.
30 S. M. J. van Duijnhoven, M. S. Robillard, K. Nicolay and H. Grüll, *Contrast Media Mol. Imaging*, 2015, **10**, 59–66.
31 Z. Fan, L. Sun, Y. Huang, Y. Wang and M. Zhang, *Nat. Nanotechnol.*, 2016, **11**, 388–394.
32 W. Xu, K. Kattel, J. Y. Park, Y. Chang, T. J. Kim and G. H. Lee, *Phys. Chem. Chem. Phys.*, 2012, **14**, 12687–12700.
33 X. Mao, J. Xu and H. Cui, *Wiley Interdiscip. Rev.: Nanomed. Nanobiotechnol.*, 2016, **8**, 814–841.
34 A. H. Hung, M. C. Duch, G. Parigi, M. W. Rotz, L. M. Manus, D. J. Mastarone, K. T. Dam, C. C. Gits, K. W. MacRenaris, C. Luchinat, M. C. Hersam and T. J. Meade, *J. Phys. Chem. C*, 2013, **117**, 16263–16273.
35 A. Semkina, M. Abakumov, N. Grinenko, A. Abakumov, A. Skorikov, E. Mironova, G. Davydova, A. G. Majouga, N. Nukolova, A. Kabanov and V. Chekhonin, *Colloids Surf., B*, 2015, **136**, 1073–1080.
36 D. Hu, Z. Sheng, G. Gao, F. Siu, C. Liu, Q. Wan, P. Gong, H. Zheng, Y. Ma and L. Cai, *Biomaterials*, 2016, **93**, 10–19.
37 J. Pan, Y. Wang, H. Pan, C. Zhang, X. Zhang, Y.-Y. Fu, X. Zhang, C. Yu, S.-K. Sun and X.-P. Yan, *Adv. Funct. Mater.*, 2017, **27**, 1603440.
38 E. Perillo, K. Hervé-Aubert, E. Allard-Vannier, A. Falanga, S. Galdiero and I. Chourpa, *J. Colloid Interface Sci.*, 2017, **499**, 209–217.
39 S. Ben Djemaa, S. David, K. Hervé-Aubert, A. Falanga, S. Galdiero, E. Allard-Vannier, I. Chourpa and E. Munnier, *Eur. J. Pharm. Biopharm.*, 2018, **131**, 99–108.
40 E. J. Chung, Y. Cheng, R. Morshed, K. Nord, Y. Han, M. L. Wegscheid, B. Auffinger, D. A. Wainwright, M. S. Lesniak and M. V. Tirrell, *Biomaterials*, 2014, **35**, 1249–1256.
41 J. Li, Y. Gao, Y. Kuang, J. Shi, X. Du, J. Zhou, H. Wang, Z. Yang and B. Xu, *J. Am. Chem. Soc.*, 2013, **135**, 9907–9914.
42 J. G. Vineberg, E. S. Zuniga, A. Kamath, Y. J. Chen, J. D. Seitz and I. Ojima, *J. Med. Chem.*, 2014, **57**, 5777–5791.
43 J. G. Vineberg, T. Wang, E. S. Zuniga and I. Ojima, *J. Med. Chem.*, 2015, **58**, 2406–2416.
44 S. M. J. Van Duijnhoven, M. S. Robillard, K. Nicolay and H. Grüll, *Molecules*, 2015, **20**, 12076–12092.
45 H. Hanaoka, T. Nakajima, K. Sato, R. Watanabe, Y. Phung, W. Gao, T. Harada, I. Kim, C. H. Paik, P. L. Choyke, M. Ho and H. Kobayashi, *Nanomedicine*, 2015, **10**, 1139–1147.
46 H. B. Na, I. C. Song and T. Hyeon, *Adv. Mater.*, 2009, **21**, 2133–2148.
47 G.-P. Yan, L. Robinson and P. Hogg, *Radiography*, 2007, **13**, e5–e19.
48 A. Puri and R. Blumenthal, *Acc. Chem. Res.*, 2011, **44**, 1071–1079.
49 P. Caravan, *Chem. Soc. Rev.*, 2006, **35**, 512–523.
50 H. J. Weinmann, R. C. Brasch, W. R. Press and G. E. Wesbey, *Am. J. Roentgenol.*, 1984, **142**, 619–624.
51 K. Micskei, L. Helm, E. Brucher and A. E. Merbach, *Inorg. Chem.*, 1993, **32**, 3844–3850.
52 Y. Kimura, R. Kamisugi, M. Narazaki, T. Matsuda, Y. Tabata, A. Toshimitsu and T. Kondo, *Adv. Healthcare Mater.*, 2012, **1**, 657–660.
53 J. Fang, P. Chandrasekharan, X.-L. Liu, Y. Yang, Y.-B. Lv, C.-T. Yang and J. Ding, *Biomaterials*, 2014, **35**, 1636–1642.
54 J. J. Yang, J. Yang, L. Wei, O. Zurkiya, W. Yang, S. Li, J. Zou, Y. Zhou, A. L. W. Maniccia, H. Mao, F. Zhao, R. Malchow, S. Zhao, J. Johnson, X. Hu, E. Krogstad and Z.-R. Liu, *J. Am. Chem. Soc.*, 2008, **130**, 9260–9267.
55 G. J. Strijkers, W. J. M. Mulder, R. B. van Heeswijk, P. M. Frederik, P. Bomans, P. C. M. M. Magusin and K. Nicolay, *Magn. Reson. Mater. Phys., Biol. Med.*, 2005, **18**, 186–192.
56 S. Langereis, Q. G. de Lussanet, M. H. P. van Genderen, E. W. Meijer, R. G. H. Beets-Tan, A. W. Griffioen, J. M. A. van Engelshoven and W. H. Backes, *NMR Biomed.*, 2006, **19**, 133–141.
57 C. Boyer, V. Bulmus, J. Liu, T. P. Davis, M. H. Stenzel and C. Barner-Kowollik, *J. Am. Chem. Soc.*, 2007, **129**, 7145–7154.
58 M. F. Wendland, *NMR Biomed.*, 2004, **17**, 581–594.
59 D. R. Martin, S. K. Krishnamoorthy, B. Kalb, K. N. Salman, P. Sharma, J. D. Carew, P. A. Martin, A. B. Chapman, G. L. Ray, C. P. Larsen and T. C. Pearson, *J. Magn. Reson. Imaging*, 2010, **31**, 440–446.
60 D. Pan, A. H. Schmieder, S. A. Wickline and G. M. Lanza, *Tetrahedron*, 2011, **67**, 8431–8444.
61 A. Skjold, B. H. Amundsen, R. Wiseth, A. Støylen, O. Haraldseth, H. B. W. Larsson and P. Jynge, *J. Magn. Reson. Imaging*, 2007, **26**, 720–727.
62 L. Zou, H. Wang, B. He, L. Zeng, T. Tan, H. Cao, X. He, Z. Zhang, S. Guo and Y. Li, *Theranostics*, 2016, **6**, 762–772.
63 J. Ruiz-Cabello, B. P. Barnett, P. A. Bottomley and J. W. M. Bulte, *NMR Biomed.*, 2011, **24**, 114–129.
64 E. N. G. Marsh and Y. Suzuki, *ACS Chem. Biol.*, 2014, **9**, 1242–1250.
65 M. Srinivas, P. Boehm-Sturm, C. G. Figdor, I. J. de Vries and M. Hoehn, *Biomaterials*, 2012, **33**, 8830–8840.
66 C. Guo, S. Xu, A. Arshad and L. Wang, *Chem. Commun.*, 2018, **54**, 9853–9856.
67 C. Zhang, S. S. Moonshi, W. Wang, H. T. Ta, Y. Han, F. Y. Han, H. Peng, P. Král, B. E. Rolfe, J. J. Gooding, K. Gaus and A. K. Whittaker, *ACS Nano*, 2018, **12**, 9162–9176.
68 I. O. Ko, K.-H. Jung, M. H. Kim, K. J. Kang, K. C. Lee, K. M. Kim, I. Noh, Y. J. Lee, S. M. Lim, J. Y. Kim and J.-A. Park, *Contrast Media Mol. Imaging*, 2017, **2017**, 3981358.
69 S. S. Moonshi, C. Zhang, H. Peng, S. Puttick, S. Rose, N. M. Fisk, K. Bhakoo, B. W. Stringer, G. G. Qiao, P. A. Gurr and A. K. Whittaker, *Nanoscale*, 2018, **10**, 8226–8239.
70 H. Wang, K. R. Raghupathi, J. Zhuang and S. Thayumanavan, *ACS Macro Lett.*, 2015, **4**, 422–425.
71 F. Zhang, Q. Zhou, G. Yang, L. An, F. Li and J. Wang, *Chem. Commun.*, 2018, **54**, 3879–3882.
72 A. V. Ratner, S. Quay, H. H. Muller, B. B. Simpson, R. Hurd and S. W. Young, *Invest. Radiol.*, 1989, **24**, 224–227.
73 M. S. Fox, J. M. Gaudet and P. J. Foster, *Magn. Reson. Insights*, 2016, **8**, 53–67.

 

74 F. Chapelin, C. M. Capitini and E. T. Ahrens, *J. Immunother. Cancer*, 2018, **6**, 105–105.
75 S. E. Kirberger, S. D. Maltseva, J. C. Manulik, S. A. Einstein, B. P. Weegman, M. Garwood and W. C. K. Pomerantz, *Angew. Chem., Int. Ed.*, 2017, **56**, 6440–6444.
76 J. C. Jackson, J. T. Hammill and R. A. Mehl, *J. Am. Chem. Soc.*, 2007, **129**, 1160–1166.
77 C. T. Gee, K. E. Arntson, A. K. Urick, N. K. Mishra, L. M. L. Hawk, A. J. Wisniewski and W. C. K. Pomerantz, *Nat. Protoc.*, 2016, **11**, 1414.
78 S. M. Dadfar, K. Roemhild, N. I. Drude, S. von Stillfried, R. Knüchel, F. Kiessling and T. Lammers, *Adv. Drug Delivery Rev.*, 2019, **138**, 302–325.
79 A. K. Gupta and M. Gupta, *Biomaterials*, 2005, **26**, 1565–1573.
80 Z. Karimi, L. Karimi and H. Shokrollahi, *Mater. Sci. Eng., C*, 2013, **33**, 2465–2475.
81 F. Chen, J. Ward and P. J. Robinson, *Magn. Reson. Imaging*, 1999, **17**, 549–556.
82 J.-Y. Choi, M.-J. Kim, J. H. Kim, S. H. Kim, H.-K. Ko, J. S. Lim, Y. T. Oh, J.-J. Chung, H. S. Yoo, J. T. Lee and K. W. Kim, *Eur. J. Radiol.*, 2006, **60**, 84–90.
83 E. Amstad, S. Zurcher, A. Mashaghi, J. Y. Wong, M. Textor and E. Reimhult, *Small*, 2009, **5**, 1334–1342.
84 M. Arruebo, R. Fernández-Pacheco, M. R. Ibarra and J. Santamaría, *Nano Today*, 2007, **2**, 22–32.
85 A. L. Miranda-Vilela, K. R. Yamamoto, K. L. C. Miranda, B. N. Matos, M. C. de Almeida, J. P. F. Longo, J. de Souza Filho, J. M. S. Fernandes, P. P. C. Sartoratto and Z. G. M. Lacava, *Tumor Biol.*, 2014, **35**, 3391–3403.
86 N. A. Kalkan, S. Aksoy, E. A. Aksoy and N. Hasirci, *J. Appl. Polym. Sci.*, 2012, **123**, 707–716.
87 B. Chertok, A. E. David and V. C. Yang, *Biomaterials*, 2010, **31**, 6317–6324.
88 C. C. Berry, S. Wells, S. Charles and A. S. G. Curtis, *Biomaterials*, 2003, **24**, 4551–4557.
89 S. R. Macewan and A. Chilkoti, *Wiley Interdiscip. Rev.: Nanomed. Nanobiotechnol.*, 2013, **5**, 31–48.
90 M. Hällbrink, K. Kilk, A. Elmquist, P. Lundberg, M. Lindgren, Y. Jiang, M. Pooga, U. Soomets and Ü. Langel, *Int. J. Pept. Res. Ther.*, 2005, **11**, 249–259.
91 A. Carvalho, M. B. F. Martins, M. L. Corvo and G. Feio, *Mater. Sci. Eng., C*, 2014, **43**, 521–526.
92 B. Valeur and M. N. Berberan-Santos, *Molecular Fluorescence: Principles and Applications*, 2nd edn, 2012.
93 T. Fisher, Fluorescent Probes: Protein Biology Resource Laboratory, https://www.thermofisher.com/us/en/home/life-science/protein-biology/protein-biology-learning-center/.
94 C. F. Liu, R. Chen, J. A. Frezzo, P. Katyal, L. K. Hill, L. Yin, N. Srivastava, H. T. More, P. D. Renfrew, R. Bonneau and J. K. Montclare, *Biomacromolecules*, 2017, **18**, 2688–2698.
95 A. C. Freise and A. M. Wu, *Mol. Immunol.*, 2015, **67**, 142–152.
96 J. A. Carr, D. Franke, J. R. Caram, C. F. Perkinson, M. Saif, V. Askoxylakis, M. Datta, D. Fukumura, R. K. Jain, M. G. Bawendi and O. T. Bruns, *Proc. Natl. Acad. Sci. U. S. A.*, 2018, **115**, 4465–4470.
97 W. Stummer, U. Pichlmeier, T. Meinel, O. D. Wiestler, F. Zanella and H. J. Reulen, *Lancet Oncol.*, 2006, **7**, 392–401.
98 R. Y. Tsien, *Annu. Rev. Biochem.*, 1998, **67**, 509–544.
99 M. Ormö, A. B. Cubitt, K. Kallio, L. A. Gross, R. Y. Tsien and S. J. Remington, *Science*, 1996, **273**, 1392.
100 D. P. Barondeau, C. J. Kassmann, J. A. Tainer and E. D. Getzoff, *J. Am. Chem. Soc.*, 2002, **124**, 3522–3524.
101 M. Mitsunaga, M. Ogawa, N. Kosaka, L. T. Rosenblum, P. L. Choyke and H. Kobayashi, *Nat. Med.*, 2011, **17**, 1685–1691.
102 E. R. Ritenour and W. R. Hendee, *Medical Imaging Physics*, John Wiley & Sons, 4th edn, 2002.
103 T. Wang, J. G. Vineberg, T. Honda and I. Ojima, *Bioorg. Chem.*, 2018, **76**, 458–467.
104 J. Kleynhans, A. F. Grobler, T. Ebenhan, M. M. Sathekge and J. R. Zeevaart, *J. Controlled Release*, 2018, **287**, 177–193.
105 I. Peñuelas, I. Domínguez-Prado, M. J. García-Velloso, J. M. Martí-Climent, M. Rodríguez-Fraile, C. Caicedo, M. Sánchez-Martínez and J. A. Richter, *J. Oncol.*, 2012, **2012**, 710561.
106 W. Wei, E. B. Ehlerding, X. Lan, Q. Luo and W. Cai, *Eur. J. Nucl. Med. Mol. Imaging*, 2018, **45**, 132–150.
107 S. Maiti and P. Paira, *Eur. J. Med. Chem.*, 2018, **145**, 206–223.
108 M. Patra, K. Zarschler, H. J. Pietzsch, H. Stephan and G. Gasser, *Chem. Soc. Rev.*, 2016, **45**, 6415–6431.
109 C. Kim, C. Favazza and L. V. Wang, *Chem. Rev.*, 2010, **110**, 2756–2782.
110 S. Bhattacharyya, S. Wang, D. Reinecke, W. Kiser, R. A. Kruger and T. R. DeGrado, *Bioconjugate Chem.*, 2008, **19**, 1186–1193.
111 A. Hannah, G. Luke, K. Wilson, K. Homan and S. Emelianov, *ACS Nano*, 2014, **8**, 250–259.
112 A. De La Zerda, C. Zavaleta, S. Keren, S. Vaithilingam, S. Bodapati, Z. Liu, J. Levi, B. R. Smith, T.-J. Ma, O. Oralkan, Z. Cheng, X. Chen, H. Dai, B. T. Khuri-Yakub and S. S. Gambhir, *Nat. Nanotechnol.*, 2008, **3**, 557.
113 X. Yang, E. W. Stein, S. Ashkenazi and L. V. Wang, *Wiley Interdiscip. Rev.: Nanomed. Nanobiotechnol.*, 2009, **1**, 360–368.
114 M. Xu and L. V. Wang, *Rev. Sci. Instrum.*, 2006, **77**, 041101.
115 D. Pan, M. Pramanik, A. Senpan, J. S. Allen, H. Zhang, S. A. Wickline, L. V. Wang and G. M. Lanza, *FASEB J.*, 2010, **25**, 875–882.
116 H. Shen, L. Zhang, M. Liu and Z. Zhang, *Theranostics*, 2012, **2**, 283–294.
117 G. Lalwani, X. Cai, L. Nie, L. V. Wang and B. Sitharaman, *Photoacoustics*, 2013, **1**, 62–67.
118 X. Lin, J. Xie, G. Niu, F. Zhang, H. Gao, M. Yang, Q. Quan, M. A. Aronova, G. Zhang, S. Lee, R. Leapman and X. Chen, *Nano Lett.*, 2011, **11**, 814–819.
119 J. M. Dominguez-Vera, *J. Inorg. Biochem.*, 2004, **75**, 3145–3157.
120 S. Gross, A. Gilead, A. Scherz, M. Neeman and Y. Salomon, *Nat. Med.*, 2003, **9**, 1327–1331.

121 P. Agostinis, K. Berg, K. A. Cengel, T. H. Foster, A. W. Girotti, S. O. Gollnick, S. M. Hahn, M. R. Hamblin, A. Juzeniene, D. Kessel, M. Korbelik, J. Moan, P. Mroz, D. Nowis, J. Piette, B. C. Wilson and J. Golab, *Ca-Cancer J. Clin.*, 2011, **61**, 250–281.

122 Y. Liu, Y. Liu, W. Bu, C. Cheng, C. Zuo, Q. Xiao, Y. Sun, D. Ni, C. Zhang, J. Liu and J. Shi, *Angew. Chem., Int. Ed.*, 2015, **54**, 8105–8109.

123 H. Chen, J. Tian, W. He and Z. Guo, *J. Am. Chem. Soc.*, 2015, **137**, 1539–1547.

124 B. Tian, C. Wang, S. Zhang, L. Feng and Z. Liu, *ACS Nano*, 2011, **5**, 7000–7009.

125 G. P. Luke, D. Yeager and S. Y. Emelianov, *Ann. Biomed. Eng.*, 2012, **40**, 422–437.

126 Z. H. Bhuiyan, C. F. Anderson and H. Cui, in *Self-assembling Biomaterials*, ed. H. S. Azevedo and R. M. P. da Silva, Woodhead Publishing, 2018, DOI: 10.1016/B978-0-08-102015-9.00025-3, pp. 533–561.

127 Y. Gou, D. Miao, M. Zhou, L. Wang, H. Zhou and G. Su, *Front. Pharmacol.*, 2018, **9**, 421.

 